

The GRAVITY fringe tracker

S. Lacour^{1,2,3}, R. Dembet^{1,4}, R. Abuter⁴, P. Fedou¹, G. Perrin¹, É. Choquet^{1,5},
O. Pfuhl², F. Eisenhauer², E. Wieprecht², T. Ott², E. Wieworrek², B. Wolff⁴,
A. Ramírez⁴, X. Haubois⁴, K. Perraut⁶, C. Straubmeier⁷, W. Brandner⁸, and A. Amorim⁹

¹ LESIA, Observatoire de Paris, Université PSL, CNRS, Sorbonne Université, Univ. Paris Diderot, Sorbonne Paris Cité, 5 place Jules Janssen, 92195 Meudon, France

² Max Planck Institute for extraterrestrial Physics, Giessenbachstraße 1, 85748 Garching, Germany

³ Department of Physics, University of Cambridge, CB3 0HE Cambridge, United Kingdom

⁴ European Southern Observatory, Karl-Schwarzschild-Straße 2, 85748 Garching, Germany

⁵ Aix Marseille Univ, CNRS, CNES, LAM, Marseille, France

⁶ Univ. Grenoble Alpes, CNRS, IPAG, 38000 Grenoble, France

⁷ 1st Institute of Physics, University of Cologne, Zùlpicher Straße 77, 50937 Cologne, Germany

⁸ Max Planck Institute for Astronomy, Königstuhl 17, 69117 Heidelberg, Germany

⁹ Universidade de Lisboa - Faculdade de Ciências, Campo Grande, 1749-016 Lisboa, Portugal

Received September 15, 1996; accepted March 16, 1997

ABSTRACT

Context. The GRAVITY instrument has been commissioned on the VLTI during 2016 and is now available to the astronomical community. It is the first optical interferometer capable of observing sources as faint as magnitude 19 in K-band. This is possible thanks to the fringe tracker which compensates the differential piston based on measurements of a brighter off-axis astronomical reference source.

Aims. The goal of this paper is to consign the main developments made in the context of the GRAVITY fringe tracker. This could serve as basis for future fringe tracking systems.

Methods. The paper therefore covers all aspects of the fringe tracker, from hardware, to control software and on-sky observations. Special emphasis is placed on the interaction between the group delay controller and the phase delay controller. The group delay control loop is a simple but robust integrator. The phase delay controller is a state-space control loop based on an auto-regressive representation of the atmospheric and vibrational perturbations. A Kalman filter provides optimal determination of the state of the system.

Results. The fringe tracker shows good tracking performance on sources with coherent K magnitudes of 11 on the UTs and 9.5 on the ATs. It can track fringes with an SNR level of 1.5 per DIT, limited by photon and background noises. On the ATs, during good seeing conditions, the optical path delay residuals can be as low as 75 nm root mean square. On the UTs, the performance is limited to around 250 nm because of structural vibrations.

Key words. Instrumentation: interferometers – Techniques: high angular resolution

1. Introduction

GRAVITY (Gravity Collaboration et al. 2017) is an instrument used on the Very Large Telescope Interferometer (VLTI) situated at the Cerro Paranal Observatory. It can combine the light from 4 telescopes. Those telescopes can either be the 4 Auxiliary telescopes (ATs, of 1.8 meter primary mirror diameter) or the 4 Unit Telescopes (UTs, of 8 meter diameter). The specifications of the instrument were derived from the most demanding science case which was to observe micro-arcseconds displacements of the light source responsible for the flares of the supermassive black hole Sgr A* (Genzel et al. 2010, and references herein). Such astrometric measurements are possible with 100 meter baselines (Shao & Colavita 1992; Lacour et al. 2014a) and were recently demonstrated on sky by Gravity Collaboration et al. (2018a,b,c).

In its quiescent state, Sgr A* can get fainter than K=18 mag. Therefore, measuring its position reliably requires an integration time of the order of minutes. To enable such long integration times it is important to correct the atmosphere effects in

real time. The higher order atmospheric wavefront distortions are compensated by an adaptive optic (AO) system. However, the AO systems do not sense, and therefore cannot correct, the differential phase between the telescopes. This is the role of the *fringe tracker*: a phase referencing target (IRS 16C in the case of Sgr A*) is used as a guide star. In real time, the optical path differences (OPD) between each pair of telescopes are computed, and are used to control the displacement of mirrors on piezoelectric systems. It is the counterpart of the AO system but at interferometric scale.

To push the comparison a little further: without fringe tracking, interferometry requires short integration times and deconvolution techniques. This was the time of Speckle imaging (Labeyrie 1970; Weigelt 1977) when using bispectrum and closure phases was a good but not really sensitive technique. With fringe tracking, optical interferometry enters a new age: long integration times (DIT up to 300 s) give access to faint sources (Kmag of 19) and to the possibility of combining spectral resolution (up to 4000) with milliarcsecond spatial resolution. This

is the historical equivalent to the emergence of adaptive optics: it enables a new level of science.

But fringe tracking is not new. Small observatories demonstrated the concept, with PTI (Colavita et al. 1999) and CHARA (Berger et al. 2006). On the Keck Interferometer (Colavita et al. 2013), comparable astrophysical objectives (Woillez et al. 2012) pushed a similar development for phase referencing (Colavita et al. 2010). Previous projects also existed at the VLTI: at first the FINITO fringe tracker (Le Bouquin et al. 2008) was used in combination with the AMBER instrument (Petrov et al. 2007). More recently ESO developed the PRIMA fringe tracker (Delplancke et al. 2006).

However, unlike AO, fringe tracking was not yet mature and important issues had to be investigated for GRAVITY. A first issue is on how to deal with limited degrees of freedom (the piston actuators) while many more optical path differences are measured (Menu et al. 2012). A second issue, which does not exist in AO, is that the phase signals are known only modulo 2π . A third issue, partially addressed by the AO community (Petit et al. 2008; Poyneer & Véran 2010) is on how to set a correct state space control system which optimally uses a Kalman filter to cancel the vibrations (Choquet et al. 2014). A fourth difficulty is the need to use both group delay (GD) and phase delay (PD) tracking in a control system to keep the best of both. The last hurdle of the project consisted in dealing with multiple closing baselines, some of them resolved. The GRAVITY fringe tracker is now the state of the art in the field of fringe tracking for optical interferometry. Below is a description of the algorithms and mechanisms.

This paper builds upon earlier works from Menu et al. (2012) and Choquet et al. (2014)¹. The first paper theoretically describes modal control of the phase delay. The second simulates the expected performance of the Kalman controller. The present paper wraps up the series by presenting the final implementation on the VLTI. Section 2 is an overview of the technical implementation of the fringe tracker, and is followed by Section 3 where the basis of the fringe sensing is defined by the observables. The control algorithm is presented in three sections: Section 4 defines the operational modes, Section 5 presents the group delay controller, and Section 6 presents the phase delay controller. Section 7 gives examples and statistics of on-sky observations. Last, Section 8 concludes the paper by a discussion on what could be improved to increase the sensitivity and accuracy of the fringe tracker.

2. Overview of the fringe tracking system

2.1. Hardware

GRAVITY is equipped with two beam combiners (Perraut et al. 2018) which perform fringe tracking and scientific observations in the K-band. GRAVITY has two main operational modes. In the on-axis mode, the light of one star is split 50:50, i.e. equal portions of the flux go to the fringe tracking and to the scientific channel. In off-axis mode, the field is split into two thanks to a roof mirror: one of the two objects serves as fringe tracking reference, while the scientific channel carries out longer integrations on the typically fainter science target (Pfuhl et al. 2010, 2012, 2014).

The two beam combiners are based on silica on silicium integrated optics (Malbet et al. 1999), optimized for $2\mu\text{m}$ observations (Jocou et al. 2010). The beam combination scheme is

¹ presented during the Final Design Review has document *VLT-TRE-GRA-15882-6701*.

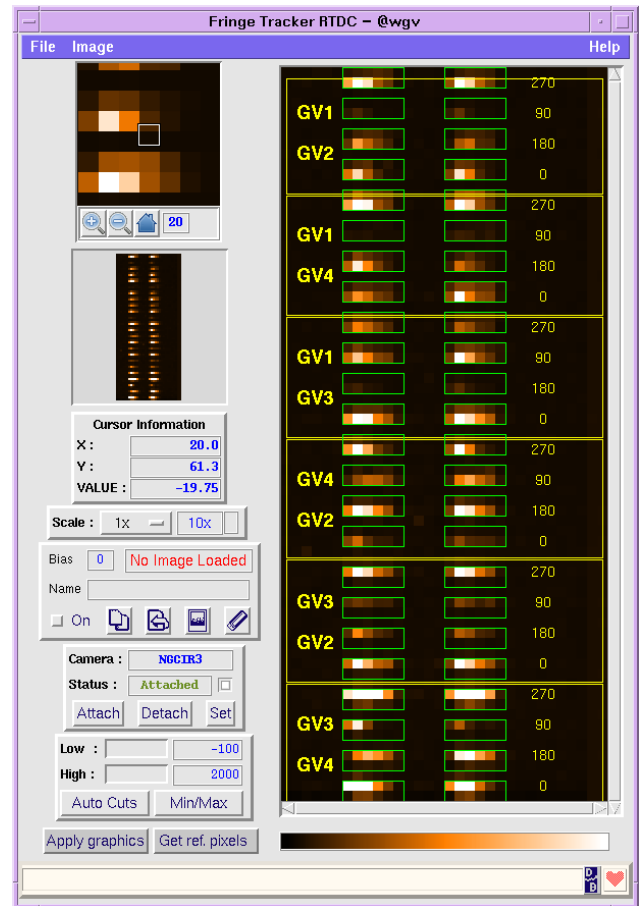


Fig. 1. RTD of the SAPHIRA detector. The pixels in the green boxes are read by the fringe tracker and used for tracking. They correspond to the 6 baselines, 4 ABCD outputs, 2 polarisations, and 6 wavelength channels. The names GV1 to GV4 correspond to the input beams. The values in yellow to the right correspond to the phase shift in degrees between the different ABCD outputs.

pair-wise. Each telescope pair is combined using a static ABCD phase modulation. This means that for each of the 6 baselines, there are four outputs corresponding to a phase shift between the two beams of $0, \pi/2, \pi$ and $3\pi/2$ radians. The total 24 output of the beam combiner can be seen on the real time display (RTD) of the instrument. These are the 24 bright lines in Fig. 1. Each one is split in two according to the two linear polarizations, and each polarization is dispersed along 6 spectral channels.

The detector is a HgCdTe avalanche photodiode array called SAPHIRA (Finger et al. 2016). It is running at either 909Hz, 303Hz, or 97Hz. It can also run either at low or high gain. The high gain corresponds to a gain of $\gamma = 7$ ADU per photo-detection with a typical readout noise below $\sigma_{\text{RON}} = 5$ ADU ($\approx 0.7 e^-$) per pixel. The low gain does not amplify the photo-detections ($\gamma = 0.5$ ADU/ e^-) and is only used for very bright targets (K magnitudes below 5 on the UTs).

The flux is processed by a first local control unit (LCU) which yields values of the observables. The LCU is an Artesyn MVME6100 using a MPC7457 PowerPC® processor (Kieckbusch et al. 2010). The data is then transmitted to a second LCU by means of a distributed memory system called Reflective Memory Network (RMN). This second LCU processes the observables to control 4 Tip/Tilt/Piston mirrors on piezoelectric actuators from Physik Instrument. Each actuator has its own position sensor, driven in closed loop. The cutoff frequency of the

piezoelectric delay lines is then above 300 Hz with a maximum optical path delay of 60 μm (Pfuhl et al. 2014).

Real time monitoring of the fringe tracking, including live display, is done on a separate Linux workstation connected to the LCUs via the RMN. This workstation processes the data, computes optimal control parameters (including the Kalman parameters), and updates the control parameters of the second LCU (Abuter et al. 2016).

2.2. Software

The two LCUs use the VxWorks operating systems. The computation is done using the TAC framework (Tools for Advanced Control) which use the standard C language environment. The TAC processing is triggered synchronously with the SAPHIRA following the predefined frequency of the detector.

The first LCU computes the necessary estimators for the controller:

- 4 flux values (F_i); see Sect. 3.2
- 6 phase delays ($\Phi_{i,j}$); see Sect. 3.3
- 6 signal-to-noise ratios ($SNR_{i,j}$); see Sect. 3.4
- 6 group delays ($\Psi_{i,j}$); see Sect. 3.5
- 4 closure phases ($\Theta_{i,j,k}$); see Sect. 3.6

Inside this LCU, only few parameters can be changed. Namely the number of DITs over which each one of these quantities can be averaged. The default values are presented in section 3.

The second LCU is in charge of controlling the piezo-mirrors for adequate fringe tracking. Figure 2 is a block diagram of the controller algorithm:

- The group delay control loop, based on an integrator controller, with a direct command to the piezo actuator (in blue).
- A feed-forward predictor, based on the action to the actuators, to increase the gain of the closed loop system (in green).
- The phase delay Kalman controller (in red).
- Two peripheral blocks for searching the fringes and adding a $\pi/2$ time modulation on the phase.

The dual architecture of the controllers is made to compromise between sensitivity and accuracy. In case of high SNR, the Kalman filter can determine and predict the states of both atmospheric and vibrational perturbation for optimal correction. In case of low SNR, the Kalman filter relies on its predictive model which, in the worst case, can be as simple as a constant value. In such a case, the group delay controller is still working efficiently, providing coherencing instead of fringe tracking.

The third and last software element is on the Linux workstation. It is a python script which runs every 5 seconds on the last 40 seconds of data calculated on the first LCU. It computes the parameters which will be used in the second LCU by the real time controller. It includes the parameters for the predictive control and the optimal gain for the Kalman filter.

3. Estimators of observables

3.1. Visibility extraction

The real time processing load consists mostly in matrix multiplications. The P2VM (for Pixel to Visibility) principle was first used for data reduction (Tatulli et al. 2007) on AMBER. AMBER used spatial modulation for fringe coding, but the formalism was subsequently adapted to work with ABCD beam combiners (Lacour et al. 2008). Using the same notation as in Lacour

et al. (2014b), the relation between the incoming electric field E_n and the outgoing electric field S_k can be expressed as:

$$S_k = \sum_n T_{k,n} E_n \quad (1)$$

where $T_{k,n}$ is the amplitude transfer function from the input n of the beam combiner to its output k . In the case of GRAVITY, $n = 4$ and $k = 24$. Averaged over the detector integration time (DIT), the flux is then equal to the average of its instantaneous intensity:

$$\langle |S_k|^2 \rangle_{\text{DIT}} = \left\langle \left| \sum_n T_{k,n} E_n \right|^2 \right\rangle_{\text{DIT}} \quad (2)$$

or, after decomposition:

$$\langle |S_k|^2 \rangle = \Re \left[\sum_n |T_{k,n}|^2 \langle |E_n|^2 \rangle + 2 \sum_n \sum_{m>n} \langle T_{k,n} T_{k,m}^* E_n E_m^* \rangle \right]. \quad (3)$$

The temporal average of the electric field leads to two kinds of coherence losses. One depends on the optical path inside the beam combiner, the other depends on the spatial brightness distribution of the astrophysical object. The first one, $C_{k,n,m}$, is intrinsic to the device and has to be calibrated. The second one, $V_{n,m}$, is the reason why we are building the interferometer. The relation with the electric field is the following:

$$\langle T_{k,n} T_{k,m}^* E_n E_m^* \rangle = \langle |T_{k,n} T_{k,m}^*| \rangle \langle |E_n E_m^*| \rangle C_{k,n,m} V_{n,m} \quad (4)$$

Hence, Eq. (3) can be written as a matrix product:

$$\begin{pmatrix} \langle |S_1|^2 \rangle \\ \vdots \\ \langle |S_{24}|^2 \rangle \end{pmatrix} = \Re \left[\mathbf{V2PM} \cdot \begin{pmatrix} \langle |E_1|^2 \rangle \\ \langle |E_2|^2 \rangle \\ \langle |E_3|^2 \rangle \\ \langle |E_4|^2 \rangle \\ \langle |E_1 E_2^*| \rangle V_{1,2} \\ \langle |E_1 E_3^*| \rangle V_{1,3} \\ \langle |E_1 E_4^*| \rangle V_{1,4} \\ \langle |E_2 E_3^*| \rangle V_{2,3} \\ \langle |E_2 E_4^*| \rangle V_{2,4} \\ \langle |E_3 E_4^*| \rangle V_{3,4} \end{pmatrix} \right] \quad (5)$$

where everything related to the transfer function of the instrument is hidden inside the V2PM matrix with 10 columns and 24 rows. V2PM is calibrated during day-time on the internal source of the instrument. It is regularly computed for verification, but has been proven to be very stable over several months. It is part of the calibration files that are needed by the first LCU (section 2.2).

P2VM is the pseudo inverse matrix of V2PM. It can be obtained by singular value decomposition and inversion of V2PM. P2VM allows to retrieve the astrophysical information from the flux observed on the pixels. This information consists in the flux F and the coherent flux Γ :

Both are computed from the pixel flux $q_{k,\lambda}$ and P2VM according to Eq (6):

$$\begin{pmatrix} F_{1,\lambda} \\ \vdots \\ F_{4,\lambda} \\ \Re[\Gamma_{1,2,\lambda}] \\ \vdots \\ \Re[\Gamma_{3,4,\lambda}] \\ \Im[\Gamma_{1,2,\lambda}] \\ \vdots \\ \Im[\Gamma_{3,4,\lambda}] \end{pmatrix} = \mathbf{P2VM}_{\lambda} \cdot \begin{pmatrix} q_{1,\lambda} \\ \vdots \\ q_{24,\lambda} \end{pmatrix} \quad (6)$$

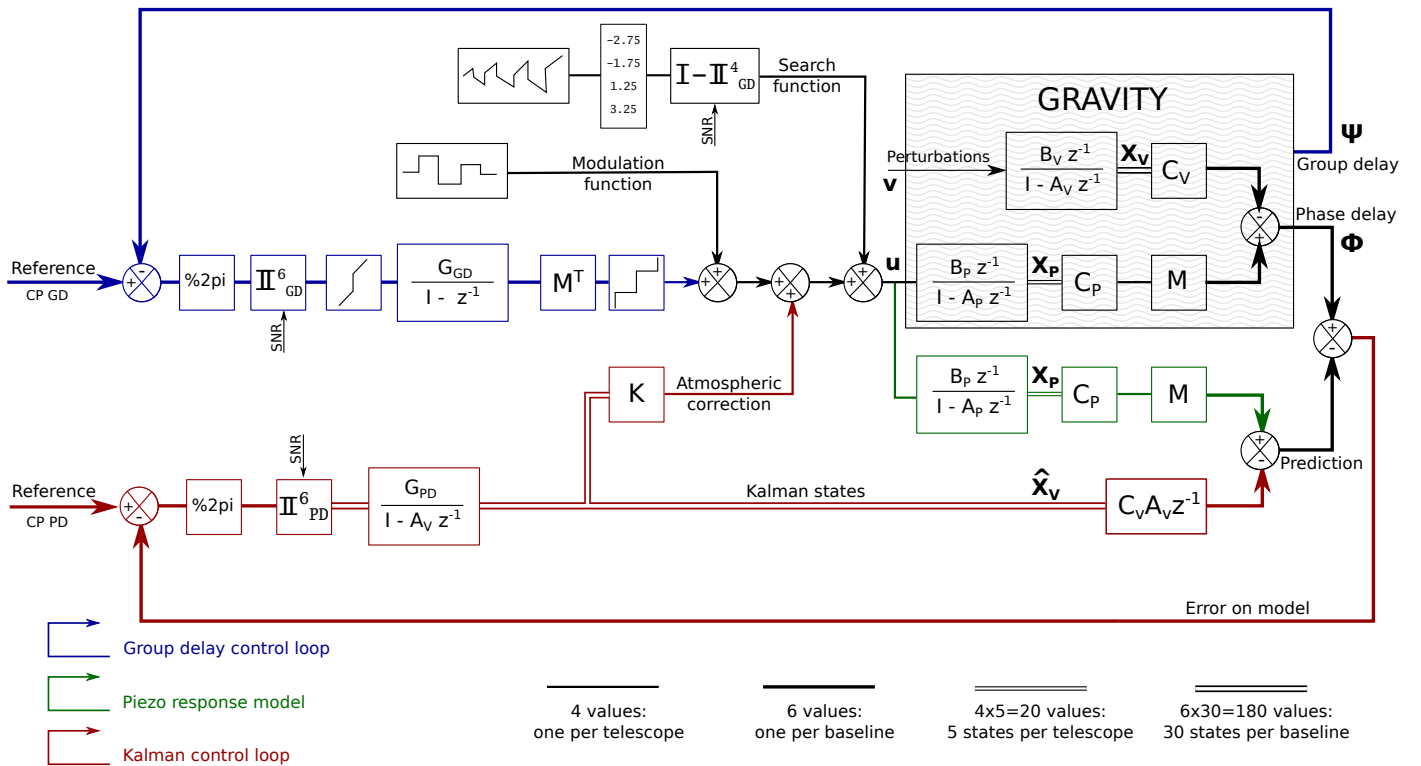


Fig. 2. Block diagram of the GRAVITY fringe tracking controller. The gray area corresponds to the GRAVITY open loop transfer function, while the rest corresponds to the two controllers. The group delay integrator controller is in blue, the phase delay state controller in red, and the actuators predictive model in green. The group delay controller is the main controller: it keeps tracking the fringes even if the instantaneous SNR is too low for phase delay tracking. The phase delay state controller is a closed loop system that determines the atmospheric perturbations $\hat{\mathbf{X}}_V$. A proportional controller (K) corrects the effect of the atmosphere.

In the above equation, we used a slightly different nomenclature, which will be used hereafter. $q_{k,\lambda} = \langle |S_{i,k,\lambda}|^2 \rangle$ is the flux over one DIT observed on a given pixel. $F_{i,\lambda} = \langle |E_{i,\lambda}|^2 \rangle$ is the flux of the incoming beam i at wavelength λ . Last, the complex coherent flux $\Gamma_{i,j,\lambda}$ corresponds to the visibility before normalization by the flux. It is obtained from the flux $F_{i,\lambda}$ and the visibilities $V_{i,j,\lambda}$:

$$\Gamma_{i,j,\lambda} = \sqrt{F_{i,\lambda} F_{j,\lambda}} \Re[V_{i,j,\lambda}] + i \sqrt{F_{i,\lambda} F_{j,\lambda}} \Im[V_{i,j,\lambda}]. \quad (7)$$

Note that all these values are computed in real time for each one of the six wavelengths in the K-band. Also in case of split polarization (when the Wollaston is inserted), the calculation is done independently for both polarizations.

3.2. Flux estimator

The flux F_i is simply the value extracted after each DIT from Eq (6), summed over the $N_\lambda = 6$ spectral channels:

$$F_i = \sum_{\lambda=1}^{N_\lambda} F_{i,\lambda} \quad (8)$$

where i corresponds to the input beam number.

3.3. Phase delay estimator

The phase delay $\Phi_{i,j}$ is derived from the complex coherent flux but after a first step to correct for the phase curvature caused by the dispersion:

$$\Gamma'_{i,j,\lambda} = \Gamma_{i,j,\lambda} \exp(iD \left[1 - \frac{2.2\mu m}{\lambda} \right]^2) \quad (9)$$

which is only a first order approximation of the dispersion. It is caused both by the atmosphere and by the fibered differential delay lines (FDDL)². . Therefore, the corrective term D is a time variable parameter which depends on the position of the star and the position of the FDDLs. The phase delay is then extracted by coherent addition of the 6 spectral channels:

$$\Phi_{i,j} = \arg(\sum_{\lambda=1}^{N_\lambda} \Gamma'_{i,j,\lambda}) \quad (10)$$

It is worth noting that the phase delay $\Phi_{i,j}$ is wrapped: it lies between $-\pi$ and π . No unwrapping effort is made at this stage.

3.4. Phase variance estimator

Computing the signal to noise ratio (SNR) of the fringes is essential for the fringe tracker. It ensures that the controller does not track on noise. It is also needed for the state machine to know if it shall start looking for fringes elsewhere. For each DIT, from the photon and background noise, the variance on each pixel is estimated:

$$Var(q_{i,\lambda}) = \sigma_{\text{skv}}^2 + \gamma(q_{i,\lambda} - q_{i,\lambda,\text{skv}}) \quad (11)$$

where σ_{sky} and $q_{i,\lambda,\text{sky}}$ are respectively the noise and flux observed during sky observations. The covariance matrix of the real and imaginary part of the Γ terms can be obtained from the

² for more info, see the GRAVITY/ESO Final Design Review document *VLT-TRE-GRA-15882-6401*.

P2VM:

$$\Sigma_{\Gamma} = \text{P2VM}_{\lambda} \cdot \begin{pmatrix} \text{Var}(q_{1,\lambda}) \\ \vdots \\ \text{Var}(q_{24,\lambda}) \end{pmatrix} \cdot \text{P2VM}_{\lambda}^{\top} \quad (12)$$

where \top is the transpose operator. To save processing time, only the diagonal values of the variance matrix are calculated. They correspond to the variance of the real and imaginary parts of $\Gamma_{i,j,\lambda}$. This assumes that the covariance between the real and imaginary parts is negligible (a good assumption for a $0, \pi/2, \pi, 3\pi/2$ ABCD). In the end, for simplicity, we estimated the variance of the phase by the following equation:

$$\text{Var}(\Phi_{i,j}) = \frac{\sum_{\lambda} \langle \text{Var}(\Re \Gamma_{i,j,\lambda}) + \text{Var}(\Im \Gamma_{i,j,\lambda}) \rangle_{5\text{DIT}}}{2 \left| \sum_{\lambda} \langle \Gamma'_{i,j,\lambda} \rangle_{5\text{DIT}} \right|^2} \quad (13)$$

which is the variance of the amplitude of the coherent flux averaged over 5 DIT. The 5 DIT average is a way to increase the precision of the calculation. It is done however at the expense of accuracy: the coherent averaging of the complex coherent flux can add a negative bias to the SNR estimator.

3.5. Group delay estimator

The group delay, $\Psi_{i,j}$, is also obtained from the complex coherent flux. Because it consists in a differential measure of the phase as a function of wavelength, this estimator is more noisy than the phase delay. To increase its signal to noise ratio, for each one of the $N_{\lambda} = 6$ spectral channels, the $\Gamma_{i,j,\lambda}$ is first corrected from dispersion, cophased, and averaged over 40 DITs. The result is then used to derive the group delay by multiplying the phasor of consecutive spectral channels:

$$\Gamma''_{i,j,\lambda} = \langle \Gamma'_{i,j,\lambda} \exp(-i\Phi_{i,j}) \rangle_{40\text{DIT}} \quad (14)$$

$$\Psi_{i,j} = \arg\left(\sum_{\lambda=1}^{N_{\lambda}-1} \Gamma''_{i,j,\lambda+1} \Gamma''_{i,j,\lambda}^*\right) \quad (15)$$

As for the phase delay, the group delay is estimated modulo 2π . But in terms of optical path, $\Psi_{i,j}$ corresponds to a value R times smaller than $\Phi_{i,j}$, with $R = 23$, the spectral resolution of the GRAVITY fringe tracker. This is explicit in open loop operation where the phase delay and group delay are compared for a response to top hat piezo commands. Because both estimators wrap at 2π , it means that the estimator is valid over a long range equal to 23 times the wavelength. This is the main advantage of the group delay estimator: to be able to find fringes far away from the central white-light fringe (the fringe of highest contrast). However, because it uses individual spectral channels, the group delay calculated on a single DIT would be extremely noisy. Thus the 40 DIT summation is a way to increase the SNR of the group delay, at the cost of losing response time.

3.6. Closure phase estimator

The closure phases, $\Theta_{i,j,k}$, are calculated on all 4 triangles from the coherent flux. Before taking the argument, the bispectra are averaged over 300 DIT (corresponding to 330 ms at the fastest 909 Hz sampling rate). Closure phases are estimated from the

phase delay:

$$\Theta_{i,j,k}^{\text{PD}} = \arg\left(\left\langle \sum_{\lambda=1}^{N_{\lambda}} \Gamma'_{i,j,\lambda} \sum_{\lambda=1}^{N_{\lambda}} \Gamma'_{j,k,\lambda} \sum_{\lambda=1}^{N_{\lambda}} \Gamma'^{*}_{i,k,\lambda} \right\rangle_{300\text{DIT}}\right), \quad (16)$$

but also from the group delay:

$$\Theta_{i,j,k}^{\text{GD}} = \arg\left(\left\langle \sum_{\lambda=1}^{N_{\lambda}} \Gamma''_{i,j,\lambda} \sum_{\lambda=1}^{N_{\lambda}} \Gamma''_{j,k,\lambda} \sum_{\lambda=1}^{N_{\lambda}} \Gamma''^*_{i,k,\lambda} \right\rangle_{300\text{DIT}}\right). \quad (17)$$

They are observables modulo 2π , no unwrapping is intended.

4. State spaces, projections & state machine

4.1. The OPD-state space

A main difficulty for the fringe tracker consists in dealing with the different dimensions of the vectors involved. The number of phase observables is 6. The number of delay lines is 4. Last, the number of degrees of freedom is 3. In Menu et al. (2012), we proposed a \mathbb{R}^3 modal-state space orthogonal to the piston space. However, as also mentioned in Menu et al. (2012), this modal control has an important drawback: it cannot work in a degraded mode where one or more telescopes are missing. Instead, the GRAVITY controller uses the OPD-state space. In some sense, the implemented fringe tracker is a downgraded version of the state controller proposed in Menu et al. (2012). However, it makes it easier to manage flux drop-out as well as working with a reduced number of baselines.

4.2. Reference vectors

For the system to work properly, the OPD-state space must be colinear to the piston space. However, because the astronomical object is not necessarily a point source, the closure phases are not necessarily zero. Therefore, the OPD component orthogonal to the piston space must be removed from the measurement. This is done by subtraction of a reference position, or set point, which is computed from the closure phase estimators $\Theta_{i,j,k}^{\text{PD}}$ and $\Theta_{i,j,k}^{\text{GD}}$. Then, the error terms, i.e. the differences between the measured OPD and the set points, are colinear to the piston space.

However, the devil is in the details. There are 4 closure phases, and only 3 can be used. So the noisiest closure phase is discarded. The three other closure phases are applied respectively on the 3 edges of the triangle forming the noisiest closure phase. The reference vector is therefore defined as:

$$\text{Ref}_{\Phi} = \begin{pmatrix} \Theta_{1,2,4}^{\text{PD}} \\ \Theta_{1,3,4}^{\text{PD}} \\ 0 \\ \Theta_{2,3,4}^{\text{PD}} \\ 0 \\ 0 \end{pmatrix} \text{ or } \begin{pmatrix} \Theta_{1,2,3}^{\text{PD}} \\ 0 \\ -\Theta_{1,3,4}^{\text{PD}} \\ 0 \\ -\Theta_{2,3,4}^{\text{PD}} \\ 0 \end{pmatrix} \text{ or } \begin{pmatrix} 0 \\ -\Theta_{1,2,3}^{\text{PD}} \\ -\Theta_{1,2,4}^{\text{PD}} \\ 0 \\ 0 \\ \Theta_{2,3,4}^{\text{PD}} \end{pmatrix} \text{ or } \begin{pmatrix} 0 \\ 0 \\ 0 \\ \Theta_{1,2,3}^{\text{PD}} \\ \Theta_{1,2,4}^{\text{PD}} \\ \Theta_{1,3,4}^{\text{PD}} \end{pmatrix} \quad (18)$$

depending on which triangle has the lowest SNR, respectively from left to right the 123, 124, 134 or 234 triangle. The reference values for the group delay are calculated similarly:

$$\text{Ref}_{\Psi} = \begin{pmatrix} \Theta_{1,2,4}^{\text{GD}} \\ \Theta_{1,3,4}^{\text{GD}} \\ 0 \\ \Theta_{2,3,4}^{\text{GD}} \\ 0 \\ 0 \end{pmatrix} \text{ or } \begin{pmatrix} \Theta_{1,2,3}^{\text{GD}} \\ 0 \\ -\Theta_{1,3,4}^{\text{GD}} \\ 0 \\ -\Theta_{2,3,4}^{\text{GD}} \\ 0 \end{pmatrix} \text{ or } \begin{pmatrix} 0 \\ -\Theta_{1,2,3}^{\text{GD}} \\ -\Theta_{1,2,4}^{\text{GD}} \\ 0 \\ 0 \\ \Theta_{2,3,4}^{\text{GD}} \end{pmatrix} \text{ or } \begin{pmatrix} 0 \\ 0 \\ 0 \\ \Theta_{1,2,3}^{\text{GD}} \\ \Theta_{1,2,4}^{\text{GD}} \\ \Theta_{1,3,4}^{\text{GD}} \end{pmatrix}$$

(19)

The closure phase will change as a function of time, making the reference position adapt to any change in the phase closures. The closure phase is smoothed over a long enough time (400 DIT) to not add additional noise. However, the choice of which triangle is the noisiest is made only once between each scientific frame to avoid sharp jumps in the reference vector over the integration time of the science detector.

This reference scheme works most of the time. However, problems will arise in two specific instances. First, when the object is so resolved that the used closure phases contain a baseline with zero visibility. If that happens, an undefined reference value will be applied to a perfectly sane baseline and the system can diverge. Second, if the fringe tracker is tracking on two unconnected baselines (for example 1-2 and 3-4), the closure phases are undefined, and using the values would mean losing one of the two high SNR baselines. To resolve these two issues, the closure phases are modified as follow: if one of the baselines of any of ij , jk or ik have an SNR below 1, then $\Theta_{i,j,k}^{\text{PD}}$ does not change while $\Theta_{i,j,k}^{\text{GD}} = 0$. The difference in treatment between the GD and PD comes from the fact that the default group delay tracking shall be zero, while the default phase delay tracking can be any constant value.

4.3. The transfer matrices

Once the reference values are subtracted from the OPD, we can freely project the data in piston-state space as well as back to the OPD-state space. Hereafter, we will use the same nomenclature as in Menu et al. (2012). \mathbf{P} corresponds to the 4-dimension piston-state vector while \mathbf{OPD} corresponds to the 6-dimension OPD-state vectors. The matrix \mathbf{M} corresponds to the conversion between piston and optical path difference:

$$\mathbf{OPD} = \mathbf{M}\mathbf{P}, \quad (20)$$

where

$$\mathbf{M} = \begin{pmatrix} -1 & -1 & -1 & 0 & 0 & 0 \\ 1 & 0 & 0 & -1 & -1 & 0 \\ 0 & 1 & 0 & 1 & 0 & -1 \\ 0 & 0 & 1 & 0 & 1 & 1 \end{pmatrix}^T. \quad (21)$$

The conversion $\mathbf{OPD} \rightarrow \mathbf{P}$ is however ill-constrained: the rank of matrix \mathbf{M} is 3, not 4. This is because the global piston cannot be obtained from the differences in the optical path. But nevertheless we can define a pseudo-inverse matrix:

$$\mathbf{M}^\dagger = \frac{1}{4} \begin{pmatrix} -1 & -1 & -1 & 0 & 0 & 0 \\ 1 & 0 & 0 & -1 & -1 & 0 \\ 0 & 1 & 0 & 1 & 0 & -1 \\ 0 & 0 & 1 & 0 & 1 & 1 \end{pmatrix}. \quad (22)$$

where † denotes the pseudo-inverse operator obtained by the mean of a Singular Value Decomposition (SVD).

4.4. Thresholds and SNR management

The system uses 2 distinct thresholds. A first threshold, σ_{GD} , disables the baselines where the SNR is too low to be useful. It is the case when the fringes are not yet found, when the fringes are suddenly lost, or when the astronomical target is so resolved that the spatial coherence is close zero. To detect these events, the σ_{GD} is compared to a moving average of the phase delay variance

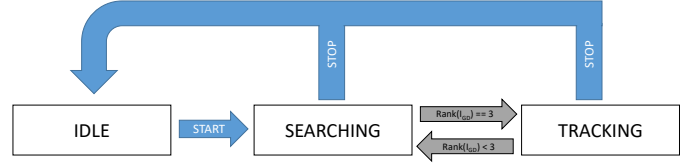


Fig. 3. State Machine of the fringe tracker. There are only three states: IDLE, SEARCHING, and TRACKING. The blue transitions are commands from the operator. The gray transitions are automatic decisions. Switching from searching to tracking only depends on the rank of the \mathbb{I}_{GD}^4 matrix. Note that if GRAVITY is running in a degraded mode the TRACKING transition can happen for a rank of 2 or even 1.

estimator: $\langle \text{Var}(\Phi_{i,j}) \rangle_{40\text{DIT}}$. This group delay threshold must be adapted to the target: it shall be high enough to ensure that the fringe tracker does not track on side-lobes, but low enough to detect the fringes.

A second threshold, σ_{PD} , is used solely for the phase tracking controller. It disables the tracking on a given telescope in case of rapid SNR drop-off. The main target of this threshold is to be able to catch a drop in flux injection (caused by external tip-tilt), with the expectation that the SNR will increase soon hereafter. Typically, $\sigma_{\text{PD}} = 1.5$ and $\sigma_{\text{PD}} < \sigma_{\text{GD}}$.

Hence, we defined two matrices \mathbb{I} which convert OPD space error into a space of same dimension collinear to the OPD space. They spell:

$$\mathbb{I}_{\text{GD}}^6 = \mathbf{M}(\mathbf{M}^T \mathbf{W} \mathbf{M})^\dagger_{\text{GD}} \mathbf{M}^T \mathbf{W} \quad (23)$$

$$\mathbb{I}_{\text{PD}}^6 = \mathbf{M}(\mathbf{M}^T \mathbf{W} \mathbf{M})^\dagger_{\text{PD}} \mathbf{M}^T \mathbf{W} \quad (24)$$

where the only difference is on the pseudo-inverse operator † . In both equations, the 6×6 weighting matrix \mathbf{W} distributes the weights among the different OPD:

$$\mathbf{W} = \text{diag} \left(\frac{1}{\sigma_{1,2}}, \frac{1}{\sigma_{1,3}}, \frac{1}{\sigma_{1,4}}, \frac{1}{\sigma_{2,3}}, \frac{1}{\sigma_{2,4}}, \frac{1}{\sigma_{3,4}} \right)^2 \quad (25)$$

where

$$\sigma_{i,j} = \begin{cases} 0 & \text{if } \langle \text{Var}(\Phi_{i,j}) \rangle_{40\text{DIT}} < \sigma_{\text{GD}}^2 \\ \sqrt{\text{Var}(\Phi_{i,j})} & \text{otherwise} \end{cases} \quad (26)$$

This step is important to remove the risk of tracking on noise: if the variance of the phase reaches that threshold, the pseudo-inverse discards that baseline in its calculation. The pseudo-inversion is done using a singular value decomposition:

$$\mathbf{M}^T \mathbf{W} \mathbf{M} = \mathbf{U} \mathbf{S} \mathbf{V} \quad (27)$$

The idea behind the SVD is that \mathbf{U} and \mathbf{V} are 2 invertible orthonormal matrices (respectively the left-singular and right-singular eigenvectors): $\mathbf{I} = \mathbf{U} \mathbf{U}^T$ and $\mathbf{I} = \mathbf{V} \mathbf{V}^T$ where \mathbf{I} is the identity matrix. \mathbf{S} is a square diagonal matrix where the values on the diagonal correspond to the square root of the eigenvalues: $\mathbf{S} = \text{diag}(s_1, s_2, s_3, 0)$. For a 4-telescope operation, 3 eigenvalues are non-zero. The number of non-zero eigenvalues will decrease if the system cannot track all telescopes.

The pseudo inverse of matrix \mathbf{S} is calculated differently for the GD and PD control loop. For the GD control loop, we have $\mathbf{S}^\dagger_{\text{GD}} = \text{diag}(s'_1, s'_2, s'_3, 0)$ where:

$$s'_i = \begin{cases} 1/s_i & \text{if } s_i > 0 \\ 0 & \text{otherwise} \end{cases} \quad (28)$$

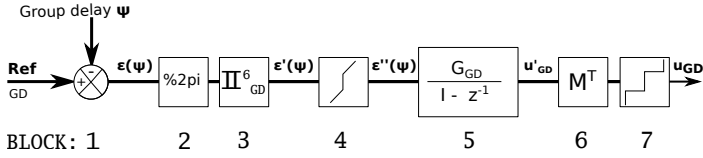


Fig. 4. Block diagram of the group delay controller. The controller is centred on an integrator (block # 5) but also includes several features to work in conjunction with the phase delay controller.

For the PD control loop, we have $\mathbf{S}^{\dagger \text{PD}} = \text{diag}(s''_1, s''_2, s''_3, 0)$ where:

$$s''_i = \begin{cases} 1/s_i & \text{if } s_i > \sigma_{\text{PD}}^2 \\ s_i/\sigma_{\text{PD}}^4 & \text{otherwise} \end{cases} \quad (29)$$

As a result, the two matrices \mathbb{I} are calculated each DIT from a new SVD and the equations:

$$\mathbb{I}_{\text{GD}}^6 = \mathbf{M}\mathbf{V}^T \mathbf{S}^{\dagger \text{GD}} \mathbf{U}^T \mathbf{M}^T \mathbf{W} \quad (30)$$

$$\mathbb{I}_{\text{PD}}^6 = \mathbf{M}\mathbf{V}^T \mathbf{S}^{\dagger \text{PD}} \mathbf{U}^T \mathbf{M}^T \mathbf{W} \quad (31)$$

where the difference between the two is that the eigenvalues in \mathbb{I}_{PD}^6 are weighted down when they are below a value equal to σ_{PD}^2 .

4.5. State machine

The rank of matrix \mathbb{I}_{GD}^6 (the number of non-zero eigenvalues) is what drives the decision-making of the state machine. For a 4-telescope operation, a rank of 3 means that the position of the delay lines on all the telescopes are constrained. If only 3 telescopes are tracked the rank is 2. The rank is 1 for 2 linked telescopes.

The state machine (Fig. 3) has therefore only three states: IDLE, SEARCHING and TRACKING. When the operator starts the fringe tracker, it switches to the state SEARCHING. As soon as the rank of the \mathbb{I}_{GD}^6 matrix is 3, the fringe tracker transition to state TRACKING. If the rank of the matrix decreases and stays low for a period of 1 s or more, then the system automatically switches back to SEARCHING mode. In both states, the group delay and phase delay controllers are running. So, whether in SEARCHING or TRACKING state, the system is still tracking the fringes on the baselines with sufficient SNR.

5. Group delay tracking

5.1. The GD block diagram

Fig. 2 represents the block diagram of the full control architecture. Within this design, the prevalent control loop is the group delay loop (in blue). It has to be very reliable: this is why the SNR on the feedback signal \mathbf{Ref}_{Ψ} is enhanced by averaging over 40 DITs. The control algorithm of the group delay is presented in Fig. 4. It is made of 7 distinct blocks which are described below.

The measured group delay is a vector defined as:

$$\mathbf{\Psi}_n = \begin{pmatrix} \Psi_{1,2} & \Psi_{1,3} & \Psi_{1,4} & \Psi_{2,3} & \Psi_{2,4} & \Psi_{3,4} \end{pmatrix}_n. \quad (32)$$

The first block is a comparator which extracts the error between a reference vector (\mathbf{Ref}_{Ψ}) and the measured group delay. The logic would be to have all 6 setpoints equal to zero to track on the white light fringes. However, as explained in Sec. 4.2, this is not possible in the presence of non-zero group delay closure phases

Θ^{GD} . So the use of a setpoint vector as defined by Eq. (19) makes sure that all baselines track the highest contrast fringes which do not conflict with each other:

$$\mathbf{\epsilon}_{\Psi,n} = \mathbf{\Psi}_n - \mathbf{Ref}_{\Psi}. \quad (33)$$

The second block is there because the phase measurement is only known modulo 2π . Since $\mathbf{\epsilon}_{\Psi,n}$ can have any value, this block will add or subtract an integer number of 2π to make sure that the error is between $-\pi$ and π .

The third block uses the \mathbb{I}_{W}^6 matrix to weight the errors between the different baselines. Following that matrix, the OPD error vector is now strictly, in a mathematical sense, colinear to the piston space. Also, the error on any baseline with no fringes is either estimated from other baselines or set to zero. After the third block, the error group delay vector is now:

$$\mathbf{\epsilon}'_{\Psi,n} = \mathbb{I}_{\text{GD}}^6 ([\mathbf{\Phi}_n - \mathbf{Ref}_{\Psi}] \% 2\pi), \quad (34)$$

where $\%$ corresponds to the modulo function.

The fourth block is a threshold function which quenches down the gain of the control loop if the absolute value of $\mathbf{\epsilon}'_{\Psi,n}$ is lower than $2\pi/R$. This value corresponds to an OPD of 1 lambda, meaning the GD controller will not try to converge to an accuracy beyond one lambda. This is necessary to let the phase delay track within a fringe:

$$\mathbf{\epsilon}''_{\Psi,n} = \begin{cases} \mathbf{\epsilon}'_{\Psi,n} - \pi/R & \text{if } \mathbf{\epsilon}'_{\Psi,n} > \pi/R \\ \mathbf{\epsilon}'_{\Psi,n} + \pi/R & \text{if } \mathbf{\epsilon}'_{\Psi,n} < -\pi/R \\ 0 & \text{otherwise} \end{cases} \quad (35)$$

The fifth block is the integrator. In the time domain, it writes:

$$\mathbf{u}'_{\text{GD},n} = \mathbf{u}'_{\text{GD},n-1} + \mathbf{G}_{\text{GD}} \mathbf{\epsilon}''_{\Psi,n} \quad (36)$$

The same controller gain \mathbf{G}_{GD} is applied to all baselines. It minimizes the closed-loop response time and maximizes robustness. The open loop transfer function is the same for each baseline. It is mostly a pure delay caused by the moving average of 40 DITs as stated by Eq. (15) in Sect. 3.5. The -3 dB cutoff frequency depends therefore on the sampling rate of the fringe tracker. It is 13, 4.5, and 1.5 Hz for sampling rates of 909, 303 and 97 Hz, respectively.

The sixth block is the matrix \mathbf{M}^{\dagger} to transpose the control signal from OPD space to piston space.

The last block is a rounding function which forces the piezo to move only by multiples of lambda. Practically, it means that the group delay controller, once it detected a group delay error larger than a fringe, will make rapid 2π phase jumps until it gets to the reference fringe, without disturbing the long term phase measurement. The command issued from the group delay controller is therefore, for each piezo actuator i , the closest value to the control signal which is a multiple of $2\pi/G_{\text{piezo}}^i$. The static gains of the piezo actuators G_{piezo}^i , in radians per Volts, are defined in section 6.2 and are calibrated beforehand. Hence:

$$\mathbf{u}_{\text{GD},n} = \text{round}_{\{2\pi/G_{\text{piezo}}^i\}} (\mathbf{M}^{\dagger} \mathbf{u}'_{\text{GD},n}). \quad (37)$$

Note that the final control signal (as shown in Fig. 2) also includes the modulation function, the fringe search function and the phase delay controller:

$$\mathbf{u} = \mathbf{u}_{\text{GD},n} + \mathbf{u}_{\text{modulation}} + \mathbf{u}_{\text{search},n} + \mathbf{u}_{\text{PD},n}. \quad (38)$$

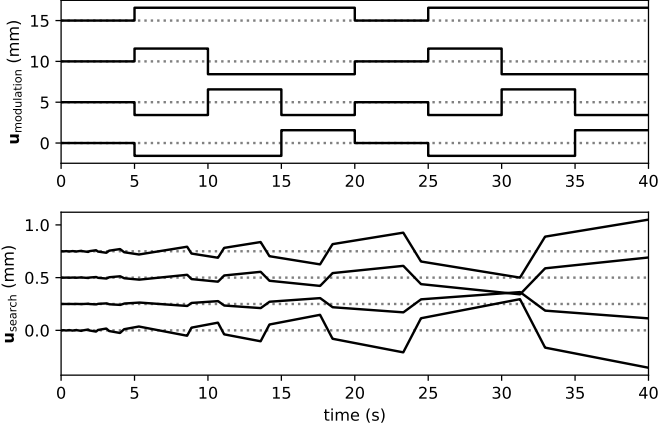


Fig. 5. Upper panel: the signal from the modulation block, in radians (the Volts to radians gain is not accounted here). Each science exposure (here 5 seconds), the $u_{\text{modulation}}$ values changes to make π offsets between the baseline. The signal repeats each 4 science exposure so each baseline is observed with as much $+\pi/2$ than $-\pi/2$ offsets. **Lower panel:** the modified sawtooth signal to search for fringes when the fringe tracker is in SEARCHING state. Here the research is made on all telescopes, meaning the rank of matrix \mathbb{I}_{GD}^6 is 0.

5.2. Modulation function and 2π phase jumps

The rounding of the group delay command ensures that the same phase is always tracked despite having to jump in between fringes when looking for the white light fringe. However, it means that the science detector will always record the fringes at the same phase delay and, for example if the sky is not well subtracted, this can bias the visibility. This can be explained in the case of a perfect ABCD beam combiner. Assuming the recorded flux on each one of the four pixel is q_A , q_B , q_C and q_D , the P2VM matrix will calculate the raw complex visibility this way:

$$V = q_A - q_C + i(q_B - q_D). \quad (39)$$

if the sky removal on q_A is not perfect, we have an additional flux which biases the measurement: $\hat{q}_A = q_A + \varepsilon_A$. To remove this error term, the solution is to record the fringes with π offsets:

$$\hat{V} = q_A + \varepsilon_A - q_C + i(q_B - q_D) \quad (40)$$

$$\hat{V}_\pi = q_C - q_A - \varepsilon_A + i(q_D - q_B) \quad (41)$$

giving:

$$V = \frac{\hat{V} + \hat{V}_\pi}{2}. \quad (42)$$

This temporal π modulation is added to the group delay command (Fig. 5). It is not seen by the GD control loop thanks to the quenching block (block number 4 in Fig. 4). This command is synchronized with the reset of the science detector, and it is sequentially:

$$u_{\text{modulation}} = \begin{pmatrix} 0 \\ 0 \\ 0 \\ 0 \end{pmatrix} \text{ or } \begin{pmatrix} \frac{\pi}{2G_{\text{piezo}}^1} \\ \frac{\pi}{2G_{\text{piezo}}^2} \\ -\frac{\pi}{2G_{\text{piezo}}^3} \\ -\frac{\pi}{2G_{\text{piezo}}^4} \end{pmatrix} \text{ or } \begin{pmatrix} \frac{\pi}{2G_{\text{piezo}}^1} \\ -\frac{\pi}{2G_{\text{piezo}}^2} \\ \frac{\pi}{2G_{\text{piezo}}^3} \\ -\frac{\pi}{2G_{\text{piezo}}^4} \end{pmatrix} \text{ or } \begin{pmatrix} \frac{\pi}{2G_{\text{piezo}}^1} \\ -\frac{\pi}{2G_{\text{piezo}}^2} \\ -\frac{\pi}{2G_{\text{piezo}}^3} \\ \frac{\pi}{2G_{\text{piezo}}^4} \end{pmatrix} \quad (43)$$

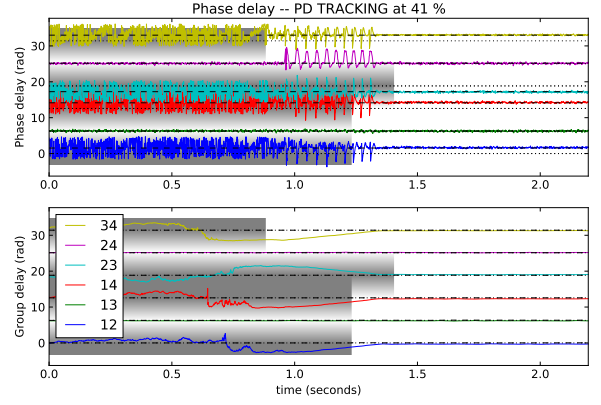


Fig. 6. Phase $\Phi_{i,j}$ (upper panel) and group $\Psi_{i,j}$ (lower panel) delays. All values are phases modulo 2π . The dashed lines correspond to the piezo command. From bottom to top, the phases correspond to baselines i, j equal to 12, 13, 14, 23, 24 and 34. At the beginning of this recording, the system has fringes on two baselines only (green and purple). At $t = 0.8$ s, the system found fringes on the yellow baseline, and later on all the other baselines. Gray areas correspond to the baselines whose SNR is below 1, meaning that no tracking is performed. After $t = 1.4$ s, the system tracks nominally on all baselines.

where G_{piezo}^i is the static gain in radian per Volts of each individual piezo i . An example of this static gain is given in Table 1. Note that a multiple of 4 science DIT with each one a $u_{\text{modulation}}$ from Eq. (43) is necessary to have, on each baseline, as many exposures with 0 and π offsets.

5.3. Fringe search

The search is done via a modified saw-tooth function of increasing amplitude (u_{saw}). This function is started when the fringe tracker goes into state SEARCHING. It is disabled when the system transition to state TRACKING. This is the only difference between the two modes. The same saw-tooth function is generated for each piezo actuator but with different scaling factors: -2.75 , -1.75 , 1.25 and 3.25 for respectively the first, second, third, and fourth beam. The four commands are then multiplied by the kernel of the \mathbb{I}_{GD}^4 matrix. This matrix is computed as:

$$\mathbb{I}_{\text{GD}}^4 = \mathbb{M}_{\text{GD}}^6 \mathbb{M}^\dagger \quad (44)$$

giving the following signal:

$$u_{\text{search},n} = (\mathbb{I}^4 - \mathbb{I}_{\text{W}}^4) \begin{pmatrix} -2.75 & -1.75 & 1.25 & 3.25 \end{pmatrix}^\top u_{\text{saw}} \quad (45)$$

where \mathbb{I}^4 is the 4×4 identity matrix. This ensures that the baselines with sufficient SNR for tracking are not modulated by the saw-tooth function. When no fringes are still found, the kernel is the identity, and each baseline is modulated. This gives the trajectory shown in Fig 5.

An example of fringe research and acquisition is presented in Fig. 6. In this example, at $t = 0$, the fringes are found and tracked on 2 baselines: the baseline between telescopes 1 and 3, and the baseline between telescopes 2 and 4. The group delay for the 2 fringes is zero, and the rank of the \mathbb{I}_{W}^4 matrix is 2. The fringe tracker is therefore in the state SEARCHING. At $t = 0.8$ s, the fringes are found on baseline 34. The rank of the \mathbb{I}_{W}^4 matrix increases, and the system switch to state TRACKING. The group delay of baselines 12, 14, 23 and 34 are brought to zero, until signals are found on all six baselines, in a nominal tracking state.

6. Phase delay tracking

6.1. Principle

The GRAVITY phase control loop uses both piston-space and OPD-space state vectors. This is the easiest way to properly handle both piezo actuators and the atmosphere dynamics (Correia et al. 2008). The vibrations and atmospheric perturbations are represented by 6 OPD-space state vectors labelled together \mathbf{x}_V . Each vector corresponds to a baseline. The piezo actuators are characterized by 4 piston-space state vectors \mathbf{x}_P , one for each delay line. The phase delay, Φ_n , is a vector of measured phases:

$$\Phi_n = \begin{pmatrix} \Phi_{1,2} & \Phi_{1,3} & \Phi_{1,4} & \Phi_{2,3} & \Phi_{2,4} & \Phi_{3,4} \end{pmatrix}_n \quad (46)$$

which results from a linear combination of the state vectors $\mathbf{x}_{V,n}$ and $\mathbf{x}_{P,n}$ at a time n .

The real time algorithm of the fringe tracker follows a sequence:

1. it predicts the future state of the system from previous states using the equation of states (Sec. 6.2)
2. it uses Kalman filtering to update the state vectors (Sec. 6.5)
3. it uses the system state to command the piezo-actuators to correct for vibrations and atmospheric effects. (Sec. 6.6)

The PD controller is summarized by the block diagram presented in Fig. 7.

6.2. Equations of state

The equations of state write:

$$\mathbf{x}_{V,n+1} = \mathbf{A}_V \cdot \mathbf{x}_{V,n} + \mathbf{B}_V \cdot \mathbf{v}_n \quad (47)$$

$$\mathbf{x}_{P,n+1} = \mathbf{A}_P \cdot \mathbf{x}_{P,n} + \mathbf{B}_P \cdot \mathbf{u}_n. \quad (48)$$

where each matrix is 3-dimensional. Because we assumed uncorrelated baselines, only the diagonals are populated:

$$\mathbf{A}_V = \text{diag} \begin{pmatrix} \mathbf{A}_V^{1,2} & \mathbf{A}_V^{1,3} & \mathbf{A}_V^{1,4} & \mathbf{A}_V^{2,3} & \mathbf{A}_V^{2,4} & \mathbf{A}_V^{3,4} \end{pmatrix} \quad (49)$$

$$\mathbf{B}_V = \text{diag} \begin{pmatrix} \mathbf{B}_V^{1,2} & \mathbf{B}_V^{1,3} & \mathbf{B}_V^{1,4} & \mathbf{B}_V^{2,3} & \mathbf{B}_V^{2,4} & \mathbf{B}_V^{3,4} \end{pmatrix} \quad (50)$$

$$\mathbf{A}_P = \text{diag} \begin{pmatrix} \mathbf{A}_P^1 & \mathbf{A}_P^2 & \mathbf{A}_P^3 & \mathbf{A}_P^4 \end{pmatrix} \quad (51)$$

$$\mathbf{B}_P = \text{diag} \begin{pmatrix} \mathbf{B}_P^1 & \mathbf{B}_P^2 & \mathbf{B}_P^3 & \mathbf{B}_P^4 \end{pmatrix} \quad (52)$$

with the upper index corresponding to the telescope or baseline numbers. In the block diagram of Fig. 2, the equations of states are written in the frequency domain, but the transfer function writes:

$$\mathcal{Z}\{\mathbf{x}_{V,n}\} = \frac{\mathbf{B}_V z^{-1}}{1 - \mathbf{A}_V z^{-1}} \mathcal{Z}\{\mathbf{v}_n\} \quad (53)$$

$$\mathcal{Z}\{\mathbf{x}_{P,n}\} = \frac{\mathbf{B}_P z^{-1}}{1 - \mathbf{A}_P z^{-1}} \mathcal{Z}\{\mathbf{u}_n\}. \quad (54)$$

The evolution of the system is driven by, on one hand, white noise \mathbf{v}_n , and, on the other hand, a user controlled voltage applied to the piezo actuators \mathbf{u}_n . Note that if \mathbf{v}_n is a white noise, $\mathbf{x}_{V,n}$ has a colored noise, as highlighted by Eq. (53). The problem is similar for adaptive optics systems, where it has already been mentioned and corrected for (Poyneer & Véran 2010).

In Menu et al. (2012) and Choquet et al. (2014), we have shown that using several autoregressive (AR) models of order 2 in parallel was effective to correct both vibration frequencies and atmospheric turbulence. However, practically, two issues made

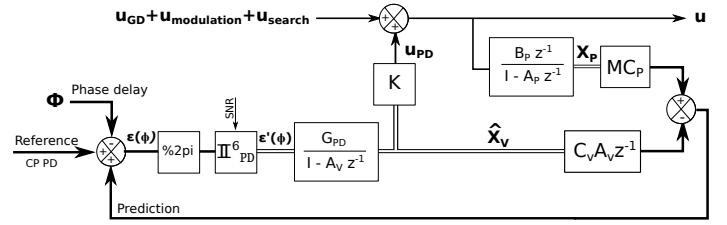


Fig. 7. Block diagram of the PD controller. The two control signals \mathbf{u}_{GD} and \mathbf{u}_{PD} are summed before being applied to the actuators. In this control scheme, it is the state vectors $\hat{\mathbf{x}}_V$ which are regulated. The control signal \mathbf{u}_{PD} is then issued from a matrix multiplication of the state vectors: $\mathbf{u}_{PD} = \mathbf{K} \hat{\mathbf{x}}_V$.

Table 1. Open loop transfer function parameters of the fringe tracker running at 909 Hz

(rad/Volts)	$i = 1$	$i = 2$	$i = 3$	$i = 4$
a_1^i	0.16	-0.03	-0.22	-0.1
a_2^i	-0.15	0.09	0.11	0.12
a_3^i	6.52	4.08	3.56	4.41
a_4^i	9.61	9.01	7.12	11.14
a_5^i	1.31	4.72	7.05	1.85
G_{piezo}^i	17.47	17.89	17.63	17.43

that implementation difficult: i) the determination of the vibration peaks for low SNR data, and ii) the need to change the space model when vibrations appear or disappear. Both problems can be technically resolved, but to ensure maximum robustness we preferred a fixed, well defined, space model. The idea is that the states \mathbf{x}_V do change with time, but the space state model does not. We used therefore an autoregressive model of order 30. It means that the state space model corresponds to the 30 last values of the phase delay:

$$\mathbf{A}_V^{i,j} = \begin{pmatrix} v_1^{i,j} & v_2^{i,j} & v_3^{i,j} & \dots & v_{29}^{i,j} & v_{30}^{i,j} \\ 1 & 0 & 0 & \dots & 0 & 0 \\ 0 & 1 & 0 & \dots & 0 & 0 \\ 0 & 0 & 1 & \dots & 0 & 0 \\ \dots & \dots & \dots & \dots & \dots & \dots \\ 0 & 0 & 0 & \dots & 1 & 0 \end{pmatrix} \quad (55)$$

and

$$\mathbf{B}_V^{i,j} = \begin{pmatrix} 1 & 0 & 0 & \dots & 0 & 0 \end{pmatrix}^T \quad (56)$$

The value of 30 allows for complexity in the vibrational pattern, while characterizing the perturbations with a sufficiently low degree of freedom. It was chosen in light of Kulcsár et al. (2012): they showed it is a good compromise with respect to other state-space models to correct atmosphere and vibration for the tip-tilt of AO systems. The transfer matrix $\mathbf{A}_V^{i,j}$ is determined each 5 seconds on a separate workstation connected on the reflective memory network.

The transmission matrix \mathbf{A}_P^i is also an autoregressive model, but of order 5. It includes the response function of the full system (image integration time, processing time, inertia of the piezo mirror, etc ...), from setting a control voltage \mathbf{u}_n to measuring a phase delay Φ_n . It is measured monthly by injecting a top-hat

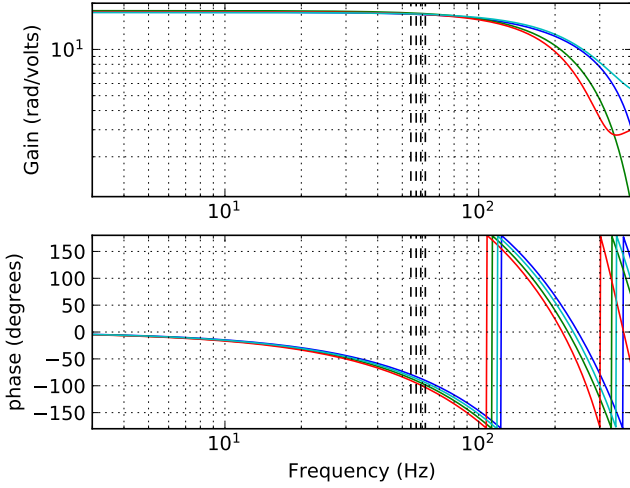


Fig. 8. Bode plot of the frequency response of the 4 pistons in open loop (including pure delay caused by integration and computation). The -90 degrees cut-off frequencies are 61Hz, 56 Hz, 54 Hz, and 59Hz. The cut-off frequency is dominated by the pure delay caused by the control loop system.

signal into the system. The matrix for the AR5 model verifies :

$$\mathbf{A}_p^i = \begin{pmatrix} a_1^i & a_2^i & a_3^i & a_4^i & a_5^i \\ 1 & 0 & 0 & 0 & 0 \\ 0 & 1 & 0 & 0 & 0 \\ 0 & 0 & 1 & 0 & 0 \\ 0 & 0 & 0 & 1 & 0 \end{pmatrix} \quad (57)$$

and

$$\mathbf{B}_p^i = \begin{pmatrix} 1 & 0 & 0 & 0 & 0 \end{pmatrix}^T \quad (58)$$

where the a_0^i , a_1^i , a_2^i , a_3^i and a_4^i values, obtained experimentally on the fringe tracker are presented in Table 1. The same values can be represented on a Bode plot, see Fig. 8. The cut-off frequencies, calculated at a phase of -90 degrees are around 60 Hz. This is considerably below the bandwidth of the piezo actuator measured by Pfuhr et al. (2010), who showed a cut-off frequency above 220 Hz. This is caused by the pure delays inside the system: detector integration time, processing time and data transfer between the different units (LCUs). The static gain of the piezo $G_{\text{piezo}}^i = \sum_{k=1}^5 a_k^i$ is also an important property of the piezo actuators because they are used both in the group and phase delay controllers.

6.3. Observation equation

The observable, Φ_n , depends on the state vectors of the piezo actuators \mathbf{x}_p and the state vectors of the atmosphere and vibrations \mathbf{x}_v . Both contribute to the phase delay. The equation for the measurement process of the phase delay is a linear combination of the two :

$$\Phi_n = \mathbf{M} \cdot \mathbf{C}_p \mathbf{x}_{p,n} - \mathbf{C}_v \mathbf{x}_{v,n} + \mathbf{w}_n + \mathbf{Ref}_\Phi \quad (59)$$

where \mathbf{w}_n is a white measurement noise and \mathbf{C}_v and \mathbf{C}_p are 3 dimensional measurement matrices with 2 dimensional matrices on the diagonal for, respectively, the vibrations and the piezo actuator:

$$\mathbf{C}_v^{i,j} = \begin{pmatrix} 1 & 0 & 0 & \dots & 0 & 0 \end{pmatrix} \quad (60)$$

$$\mathbf{C}_p^i = \begin{pmatrix} 1 & 0 & 0 & 0 & 0 \end{pmatrix} \quad (61)$$

In the case of a resolved astronomical target, the phase delay vector Φ_n also includes a term which corresponds to the spatial signature of the target on the phase. It appears in the form of a non-zero closure phase ($\Theta^{\text{PD}} \neq 0$), and is included in the phase delay by the term \mathbf{Ref}_Φ as defined in Eq. (18).

6.4. Parameter identification

The $a_{1 \leq k \leq 5}$ predictive terms for each of the piezo actuators are determined offline during dedicated calibration laboratory measurements. This is not the case for the identification of the $v_{1 \leq k \leq 30}$ AR values. They are calculated on a distinct linux workstation. The workstation is sensing in real time the phase delay passing by the reflective network. It collects each 5 seconds the last 40 seconds of data (36000 sample at 909 Hz) and computes the pseudo open loop phase delay $\Phi_{\text{ATM},n}$ by removing the influence of the piezo command and closure phases. This phase delay corresponds to the phase delay produced by the atmosphere and the vibrations only:

$$\Phi_{\text{ATM},n} = \Phi_n - \mathbf{M} \cdot \mathbf{C}_p \mathbf{x}_{p,n} - \mathbf{Ref}_\Phi \quad (62)$$

from which it calculates the differences between consecutive values:

$$\Delta \Phi_{\text{ATM},n} = \Phi_{\text{ATM},n} - \Phi_{\text{ATM},n-1} \quad (63)$$

The $\Delta \Phi_{\text{ATM},n}$ differential phase values are then processed baseline after baseline to derive 29 $p_{1 \leq i \leq 29}$ AR parameters that best represent the data. This uses the Python toolbox "Time Series Analysis". The parameters generated ensure stationarity (Jones 1980) and thus provide stability to the closed loop algorithm. Last the $v_{1 \leq i \leq 30}$ values are determined via:

$$v_i = p_i - p_{i-1} \quad (64)$$

after which the matrices \mathbf{A}_v and \mathbf{A}_p are sent by the RMN to the real time LCU to adjust the parameters of the phase delay controller.

6.5. Asymptotic Kalman filter

The vectors $\hat{\mathbf{x}}_{v,n|n-1}$ correspond to our best estimation of the state of the vibrations at a moment n from all the measurements available up to a time $n-1$. It can be estimated from $\hat{\mathbf{x}}_{v,n-1}$ according to the equation of state spelled in Eq. (47):

$$\hat{\mathbf{x}}_{v,n|n-1} = \mathbf{A}_v \cdot \hat{\mathbf{x}}_{v,n-1} \quad (65)$$

However, the goal of the Kalman filter is to update this estimation from the error between the new observable and this new estimation. This error can be derived from the measurement process spelled in Eq. (59) and writes:

$$\boldsymbol{\varepsilon}_{\Phi,n} = \mathbf{Ref}_\Phi - \Phi_n + \mathbf{M} \cdot \mathbf{C}_p \mathbf{x}_{p,n} - \mathbf{C}_v \cdot \hat{\mathbf{x}}_{v,n|n-1}, \quad (66)$$

which becomes, after unwrapping between $-\pi$ and π and baseline weighting:

$$\boldsymbol{\varepsilon}'_{\Phi,n} = \mathbb{I}_{\text{PD}}^6 \cdot ([\boldsymbol{\varepsilon}_{\Phi,n}] \% 2\pi). \quad (67)$$

where $\% 2\pi$ corresponds to modulo 2π . The \mathbb{I}_{PD}^6 matrix is here for two purposes. The first one is to derive the errors on low SNR

baselines thanks to the baselines with higher SNR. The second purpose is to make sure that the low SNR data is either weighted down or discarded thanks to the weighted pseudo inversion in Eq. (29). The state estimator $\hat{\mathbf{x}}_{V,n}$ is finally updated thanks to an integrator:

$$\hat{\mathbf{x}}_{V,n} = \mathbf{A}_V \hat{\mathbf{x}}_{V,n-1} + \mathbf{G}_{PD} \cdot \boldsymbol{\varepsilon}'_{\Phi,n}. \quad (68)$$

The gain \mathbf{G}_{PD} is not a scalar but a 3-dimensional matrix. The correct estimation of \mathbf{G}_{PD} is the basis of Kalman filtering. In GRAVITY, it is not identified each DIT, but each 5 seconds on the sensing Kalman workstation. Therefore, it is obtained from the asymptotic Kalman equations. It is calculated from the two covariance matrices of the measurement noise Σ_w and the steady state error Σ_∞ (Poyneer & V  ran 2010; Menu et al. 2012):

$$\mathbf{G}_{PD} = \Sigma_\infty \mathbf{C}_V^\dagger (\mathbf{C}_V \Sigma_\infty \mathbf{C}_V^\dagger + \Sigma_w)^{-1} \quad (69)$$

The steady state covariance matrix can be obtained from the algebraic Riccati equation, the vibrations input noise, and the vibration and atmospheric noise Σ_v :

$$\Sigma_\infty = \mathbf{A}_V \Sigma_\infty \mathbf{A}_V^\dagger - \mathbf{A}_V \Sigma_\infty \mathbf{C}_V^\dagger (\mathbf{C}_V \Sigma_\infty \mathbf{C}_V^\dagger + \Sigma_w)^{-1} \mathbf{C}_V \Sigma_\infty \mathbf{A}_V^\dagger + \Sigma_v \quad (70)$$

The noise characteristic (Σ_v, Σ_w) makes the Kalman filter optimally adapted to the average noise on the system, but not to instantaneous noise variations. Adaptability is the role of the \mathbb{I}_{PD}^6 matrix in Eq. (67).

6.6. Determination of the control signal

To use the Kalman filter as a controller an optimal command is needed. The purpose of this section is to determine the control signal $\mathbf{u}_{PD,n}$ from the atmospheric state vectors : $\mathbf{u}_{PD,n} = \mathbf{K} \hat{\mathbf{x}}_V$. The task of this signal is twofold. First, it must cancel the atmospheric perturbations on the measured phase delay ($\Phi_{ATM,n}$). Second, it must ensure that the phase delay converges to the group delay control signal $\mathbf{u}_{GD,n} + \mathbf{u}_{modulation} + \mathbf{u}_{search,n}$.

The first task uses the predictive power of the equation of states:

$$\mathbf{u}_{PD,n} \propto \mathbf{M} \mathbf{C}_V \mathbf{A}_V^{n_{DIT}} \hat{\mathbf{x}}_V \quad (71)$$

where $\mathbf{A}_V^{n_{DIT}}$ is the power of matrix \mathbf{A}_V over n_{DIT} samples. The integer n_{DIT} is there to account for the delay between control signal and its effect on the phase delay. Ideally $n_{DIT} = 1$ but because of the pure delay in the open loop transfer function it must be higher. This pure delay depends on the frequency of the fringe tracker. We are currently using $n_{DIT} = 3$ for the 909 Hz frequency and $n_{DIT} = 2$ for the lowest frequencies.

The second task is achieved thanks to the integrator in Eq. (68). This integrator makes sure that the vector states of atmospheric perturbations are always up to date. It tries to get the quantity $\boldsymbol{\varepsilon}_{\Phi,n}$ as close as possible to zero. If $\boldsymbol{\varepsilon}_{\Phi,n} = 0$, it is possible to have $\Phi_n = \mathbf{G}_{piezo}^{-1} (\mathbf{u} - \mathbf{u}_{PD,n})$ if the control signal is:

$$\mathbf{u}_{PD,n} = -\mathbf{G}_{piezo}^{-1} \mathbf{M} \mathbf{C}_V \mathbf{A}_V^{n_{DIT}} \hat{\mathbf{x}}_V. \quad (72)$$

The \mathbf{G}_{piezo}^{-1} matrix is diagonal and corresponds to the ratio between the phase delay and the applied voltage to the piezo actuators:

$$\mathbf{G}_{piezo}^{-1} = \text{diag} \left(\frac{1}{G_{piezo}^1}, \frac{1}{G_{piezo}^2}, \frac{1}{G_{piezo}^3}, \frac{1}{G_{piezo}^4} \right) \quad (73)$$

where G_{piezo}^i corresponds to the static gain of each piezo actuator as described in section 6.2 (values for 909 Hz tracking are presented in Table 1).

6.7. Why not a simpler state controller?

The block diagram presented in Fig. (2) shows the complexity of the fringe tracker. A simpler version was used during the first commissioning in 2016. Both the phase and group delay controller were different. First, the group delay control signal was not used to directly command the piezo actuators but instead it was used as a setpoint for the phase delay controller. Second, the phase delay controller was a proportional-integral controller. It was efficient and robust and a good commissioning tool. However, at low SNR, its performance was not adequate. The reasons were:

- the phase delay estimator is noisy. The proportional controller (or worse, a derivative) was injecting directly the noise back into the control signal. This was especially problematic during flux dropouts when the SNR can be close to zero.
- the phase delay is modulo 2π . It needs to be unwrapped with respect to a prediction. Using the setpoint as the prediction was resulting in many fringe jumps during bad atmospheric conditions.

In consequence of that, we decided to skip the phase delay proportional controller and have the group delay directly command the piezo, without feedback from the phase delay. In parallel to the group delay controller, we included a Kalman filter on the phase delay feedback, and used the predictive model to unwrap the phase (the vector $\boldsymbol{\varepsilon}'_{\Phi,n}$). This gave the block diagram in Fig. 7.

7. On sky observations

7.1. Operation

The simplicity to operate the fringe tracker lies in the simplicity of the state machine. With only three states, the operator interactions are limited to the transition between IDLE, SEARCH and back to IDLE. Once the fringes are detected, the system will switch automatically to TRACKING and the instrument will then start recording data. However, there are two free parameters that could ask for the intervention of the operator: the σ_{GD} and σ_{PD} thresholds. The typical error for example is to set a σ_{GD} too low and risk the tracking on the second lobe of a fringe packet.

Once the thresholds are correctly set, the system is made to be fully autonomous, and able to deal with any glitch of the VLTI. For example, Fig. 9 shows the fringe tracker losing telescope AT2 and how it recovered. The figures are the same plots as the ones available to the support astronomer during real time GRAVITY operation. The data were captured and plotted at $t = 0$ s. At $t = -6.39$ s the AT2 loose its pointing target, and the injected flux in the fiber drops. Immediately, the SNR level drops below the purple line, and the FT gives up tracking on all the three baselines that include AT2. At this point, the system is still in state TRACKING. At $t = -5.39$ s, after a time delay of 1 second, the system switches to state SEARCHING, and the VLTI delay lines start following the sawtooth function. At $t = -3.26$ s the system recovers the fringes on the AT2-AT1 baseline and starts centring them. At this point, the rank of the \mathbb{I}_w^4 matrix is back to 3 and the fringe tracker switches back to the TRACKING state. At $t = -3.12$ s the fringes are detected on all 6 baselines and the system tracks again nominally.

In summary, the complexity of dealing with multiple baselines is hidden behind the \mathbb{I}_{GD} and \mathbb{I}_{PD} matrices presented in Sec. 4.4. From the user point of view, the fringe tracker transitions from state SEARCHING to state TRACKING, but the engine behind the scene does not change the way it operates.

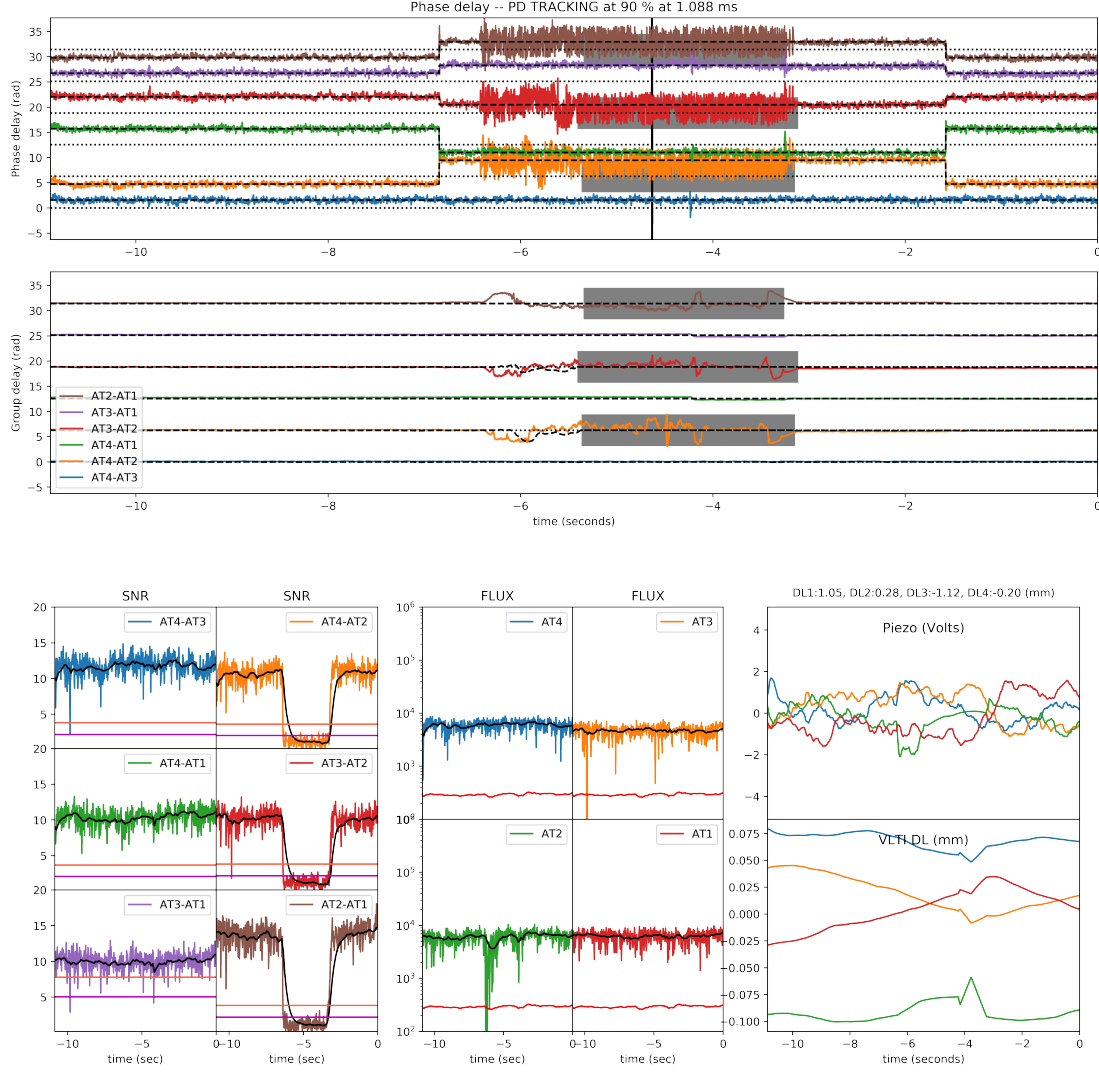


Fig. 9. Observation of star GJ 65 A on November 21th 2018. This example shows the case of a glitch on AT2 adaptive optics system which resulted in the loss followed by the recovery of the fringe by the fringe tracker. **Upper 2 panels:** the fringe tracker phase $\Phi_{i,j}$ and group delay $\Psi_{i,j}$ estimators. The color lines correspond to each one of the six baselines. The $\pi/2$ phase jumps at -7 and -1.5 seconds are normal and correspond to the modulation synchronised with the 5s DIT science camera (the high spectral resolution detector). The gray areas correspond to detection of low SNR fringes by the controller. **Lower left panels:** The SNR for each one of the baselines calculated as $1/\sqrt{\text{Var}(\Phi_{i,j})}$. The horizontal red lines correspond to the GD threshold ($1/\sigma_{GD}$). The horizontal purple lines correspond to the PD threshold ($1/\sigma_{PD}$). If the black line goes below the red line the FT stop tracking on that baseline. **Lower center panel:** the flux F_i . Similarly, the red line is a threshold made by a moving average of all flux which will detect the loss of a telescope. **Lower right panels:** commands to the piezo actuators and VLT delay line actuators. The piezo actuators take care of the fast control signal while the VLT delay line are used to offload and to search for fringes over large distances.

7.2. Sensitivity

The sensitivity is mostly a question of having enough photons on the detector to generate a feedback signal for the fringe tracker. In Fig. 10 are plotted the flux versus magnitude of calibrators observed with GRAVITY during a period covering June 2017 to November 2018. The selection of the files with a tracking ratio above 80% leads to a total of 1117 exposures on 473 distincts calibrators. The orange dots correspond to the 814 AT observations. The others correspond to the MACAO (visible AO) and CIAO (infrared AO) UTs observations. The solid lines correspond to a total transmission of 1% from telescope to the fringe tracker detector. The dashed lines correspond to the theoretical detector noise, scaled by $\sqrt{N_p}$, with N_p the total number of pixels divided by the number of telescopes.

On the ATs, to date, the faintest target observed was TYC 5058-927-1, a star with $K = 9.4$ mag. It was observed during the night of the 5th April 2017 when the atmospheric conditions were excellent: seeing down to $0.4''$ and coherence time up to 12 ms. The observations were done in single field mode, where only half the flux is sent to the fringe tracker. The fringe tracker was efficiently tracking the fringes 100 % of the exposure time, at a frequency rate of 97 Hz, with OPD residuals between 250 and 350 nm.

Technically, if we were to extrapolate to the UTs the sensitivity observed on the ATs, we should be able to track stars of K magnitudes up to 12.5. However, to date, the faintest star observed with the fringe tracker on the UTs is TYC 7504-160-1, a star with $K = 11.1$ mag. It was observed during the night of the 2nd July 2017 during good atmospheric condition: seeing

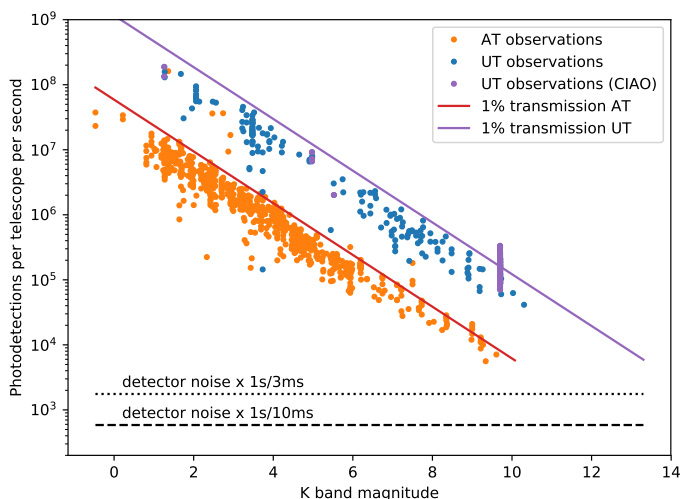


Fig. 10. Transmission plot, i.e., photons detected on the GRAVITY FT receiver, per telescope and per second, as a function of the K-band magnitude (tracking ratio $> 80\%$). The magnitudes of the targets are obtained from SIMBAD. Most of the observations are done on-axis, meaning that 50% of the flux is lost because of the beam splitter. However, the many $K=9.7$ mag CIAO observations are taken off-axis, hence the higher flux. Targets observed with ATs can be as faint as 10 magnitudes. From this plot, because the flux observed with the UTs is more than 10 times higher, observations shall be possible up to magnitude 13. However, there has been no observations at magnitudes higher than 11.1.

between $0.4''$ and $0.6''$, coherence time between 4 and 7 ms. The frequency rate was of 303 Hz, with OPD residuals between 350 and 400 nm.

The relatively low UT sensitivity is still not understood. One explanation could be that the 97 Hz integration time is not usable: the fringe contrast is attenuated by the vibrations of the UT structure. Another explanation could come from moderate AO performances. With a low Strehl, difficulties to inject the light in the fibers decrease the number of photons available, but also create flux drops which decrease the visibility and complicate the fringe tracking. One last possibility is a selection effect caused by the lower availability of the UTs.

7.3. Signal to noise

The limit for fringe tracking should be, in theory, an SNR of 1 per DIT. However, from experience, we observed that an SNR of 1.5 is needed for proper fringe tracking.

The signal consists in the number of coherent photon received. The noise is created by quantum noise on one hand and the background noise on the other hand. At 909, 303 and 97 Hz, we measured respectively during sky observation $\sigma_{\text{sky}} = 4, 5$ and 8 ADU per pixel. These values are coherent with a quadratic sum of noise coming from metrology scattered light (7 ADU at 97 Hz), sky and environmental background (6 ADU at 97 Hz) and read-out noise (4 ADU).

The detector variance observed during sky observations is used to compute the real time SNR shown in the lower left panel of Fig. 9. In Fig. 11, for a dataset covering the 7 months between April and November, we have plotted this SNR as a function of the measured flux. The three solid lines correspond to the theoretical SNR calculated from σ_{sky} and photon noise. The fact that the values lie below these theoretical lines is due to a loss of visibility contrast. It can be caused either by non-equilibrium of

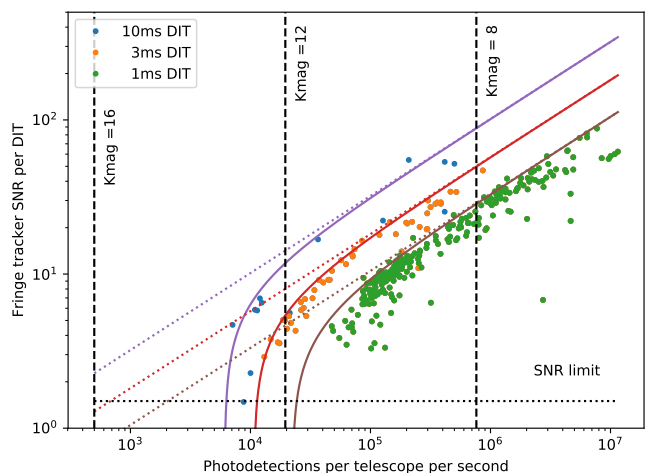


Fig. 11. SNR as a function of detected photon per telescope per DIT. The SNR is the one computed by the real time computer, defined by $1/\sqrt{\text{Var}(\Phi_{i,j})}$ as stated in Eq. (13). The three colors correspond to the 3 different frame rates of the fringe tracker. The solid lines correspond to theoretical values assuming 100 % fringe contrast. The vertical lines are theoretical flux assuming observations on UTs with 1 % throughput. The horizontal line correspond to an SNR of 1.5.

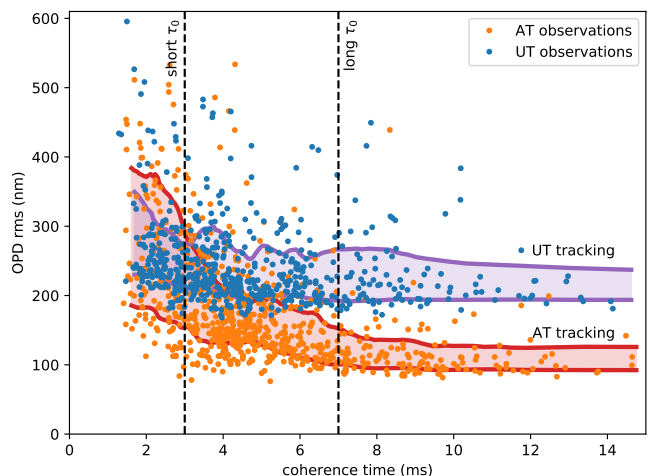


Fig. 12. OPD residuals as a function of coherence time (at 500 nm) for all calibrators and GC data taken between July 2017 and November 2018 in the 909 Hz mode. The dashed vertical lines correspond to the first quintile (3 ms) and last quintile (7 ms) of the coherence time distribution as observed by the ESO astronomical site monitor (ASM). The thick lines correspond to the first and last quintile of the OPD residuals distribution (purple for UTs and red for ATs). The median OPD residuals are 150 nm on the ATs, and 250 nm on the UTs.

the flux between the different telescopes, or by OPD variations within a DIT of the detector.

The vertical lines correspond to the flux of a star of K magnitude of 8, 12 and 16 observed with the UTs under the assumption of 1% throughput. The drop at low flux of the theoretical SNR curves correspond to the effect of the observed sky noise. This noise is mostly detector noise at high frequency, and a combination of background and metrology noise at low frequency. The dotted lines are theoretical computations of the noise assuming only photon noise. Under that assumption, 1% throughput, and 100% visibilities, the UT sensitivity could technically reach magnitudes up to $K = 16$ mag.

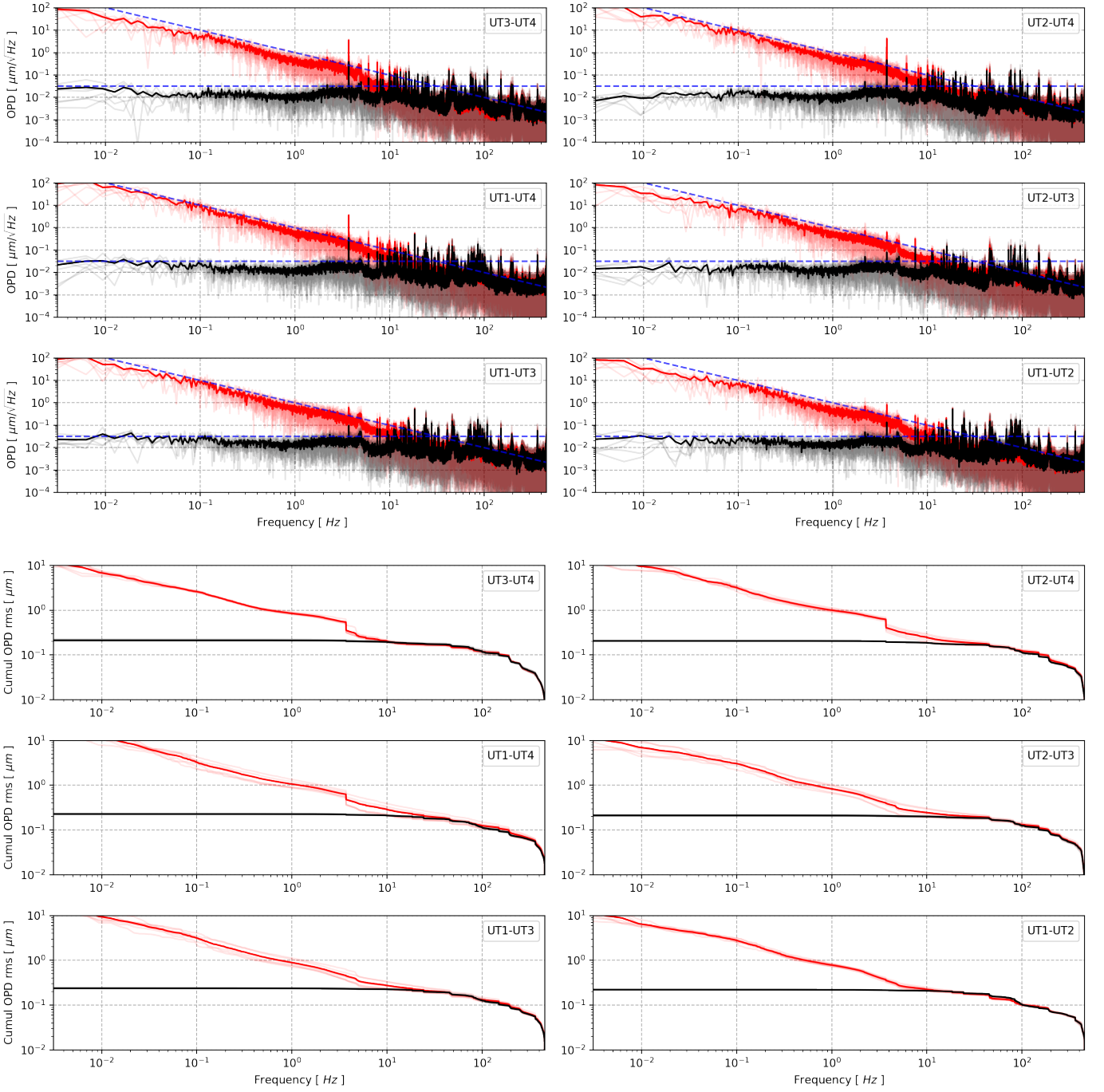


Fig. 13. Power spectrum density and cumulative sum of the power spectrum density of phase residuals ($2.2 \mu\text{m}/2\pi \times \Phi_n$) toward target IRS 16C. The red curves are the pseudo open loop values, ie, in the hypothesis of no fringe tracker ($2.2 \mu\text{m}/2\pi \times \Phi_{\text{ATM},n}$). The blue curves correspond to power spectral densities of $1 f^{-2} \mu\text{m}^2/\text{Hz}$ and $0.001 \mu\text{m}^2/\text{Hz}$. The six lower plots are the reverse cumulative sum of the power spectrum. At zero frequency, the sum reach 220 nm in average over the 6 baselines.

7.4. OPD residuals

The accuracy of the fringe tracking depends on many parameters: the faintness of the source, the wind speed, the seeing conditions and the coherence time (τ_0). For bright enough targets, we have nevertheless showed that the strongest correlation is observed with the coherence time (Lacour et al. 2018).

Using the same dataset as in Fig. 10, and using only the calibrators observed at 909 Hz, we plotted in Fig. 12 the OPD residuals as a function of the coherence time as observed by the ESO site monitor at 500 nm. On average the ATs perform better, with

a median residual of 150 nm. During the best conditions the OPD residuals can be as low as 75 nm. The UTs residuals are higher, with a median value of 250 nm, and a minimum at 180 nm.

Depending on the seeing conditions, the fringe tracker shows different limitations. During the 20% worst atmospheric conditions ($\tau_0 < 3$ ms), the UTs and ATs performance are limited by the coherence time of the atmosphere. Under these conditions, 20% of all observations have OPD residuals above 380 nm. The consequence is then that the jitter of the phase will significantly impact the visibility observed on the science channel with long

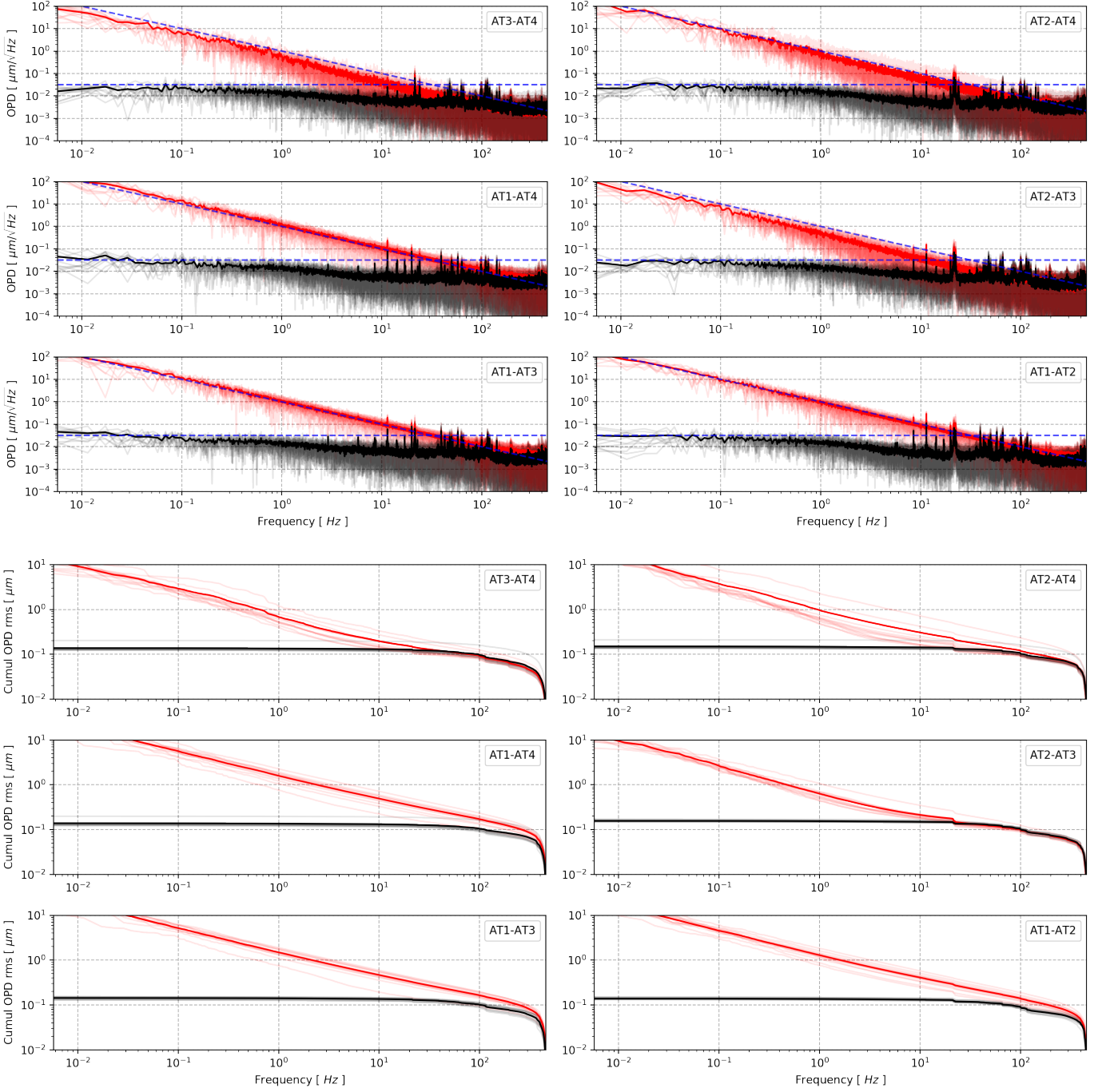


Fig. 14. Idem as in Fig 13 except for the binary star GJ 65 observed with the Auxiliary Telescopes. The fringe tracking residuals are 140 nm, smaller than what is observed on the UTs. The main difference lie in the lower level of vibrations in the 10-100 Hz range.

integration time. We can show that this loss in contrast can be directly estimated from the variance of the phase according to the relation:

$$V_{\text{residuals}} = 1 - \langle \exp(i\Phi) \rangle = 1 - \exp(-\sigma_\Phi^2/2). \quad (74)$$

With 380 nm rms jitters ($\sigma_\Phi \approx 1.1$ rad), the contrast of the fringes decreases by 45%.

During the 20% best atmospheric conditions ($\tau_0 > 7$ ms), however, the fringe tracker can reach very small residual. On the ATs, 80% of all observations are below 140 nm ($V_{\text{loss}} < 7\%$). However, on the UTs, the environmental vibrations make resid-

ual stay between 220 and 320 nm. The explanation is on the higher level of vibrations observed on the UTs.

7.5. Power spectral densities

In Fig. 13 and Fig. 14 are showed the power spectral density of the OPD for 2 astronomical objects: IRS 16C observed with UTs and GJ 65 observed with the ATs. The conditions of the observations are presented Table 2. The IRS 16C galactic center target was observed with the CIAO off-axis adaptive optics. The conditions were good to excellent, and the residual OPD around 220 nm over the entire duration of the observations. The GJ 65

Table 2. GRAVITY dataset

Object Configuration	MJD	FT freq. K mag	Seeing	τ_0 (ms)
IRS 16C	58209	909 Hz	0.4''	0.007
UT1-UT2-UT3-UT4		9.7		
GJ 65 A (&B)	58367	909 Hz	0.6''	0.006
A0-G1-J2-K0		5.7 (5.9)		

binary was also observed during good seeing conditions, without AO, and OPD residuals of 140 nm.

To compute the power spectral density, the phase delay Φ_n is unwrapped and the $\pi/4$ modulation function removed. The pseudo open loop phase delay $\Phi_{\text{ATM},n}$ is then computed from Eq. (62) using the piezo transfer function estimated during calibration. In Fig. 13 and Fig. 14 the 6 upper plots correspond to the square root of the power spectrum density. The black curves correspond to the measured OPD estimated from the phase delay Φ and the red curves is the power spectrum of the reconstructed atmosphere $\Phi_{\text{ATM},n}$. The atmospheric power spectrum (which also includes the vibrations) shows, as expected, the prevalence of the low frequencies in the atmospheric perturbations. Below 10 Hz, the power spectral density fits very well the relation:

$$\text{PSD}_{\Phi_{\text{ATM},n}}(f < 10 \text{ Hz}) = 1 f^{-2} \mu\text{m}^2/\text{Hz}. \quad (75)$$

which is not far, but different, from the power of $-5/3$ of a Kolmogorov type atmosphere. After fringe tracking correction, the residual OPD are attenuated below the spectral density:

$$\text{PSD}_{\Phi_n}(f < 10 \text{ Hz}) \leq 0.001 \mu\text{m}^2/\text{Hz}. \quad (76)$$

The fringe tracker is therefore clearly a high pass filter. The cut-off frequency of the fringe tracker correction is not well defined because it depends on the efficiency of the Kalman filter and the accuracy with which the equations of states reflect the system. On the UTs, the 3 dB cut-off frequency is of the order of 10 Hz. On the ATs, maybe because the vibrations are less present and the predictive model more accurate, the fringe tracker performance has a higher cut-off frequency at 30 Hz. This 30 Hz shows that the system is optimised because it is close to the cut-off frequency of the open loop system (≈ 60 Hz in Fig. 8).

8. Discussion

8.1. Have we reached the ultimate sensitivity?

It is often assumed that the sensitivity of an optical interferometer must decrease as a function of the number of telescopes. This is not necessarily true. The limiting sensitivity is when each one of the degrees of freedom of the fringe tracker reaches a variance of one during one coherence time of the atmosphere. And each one of the degrees of freedom corresponds to a non-zero eigenvalue of matrix \mathbb{I} (Section 4.4). This is why the threshold on the phase delay control loop (σ_{PD}) is applied on the eigenvalues in Eq. (29).

So for $N \gg 1$, the signal grows like the flux ($\propto N$), the degrees of freedom like N , and the number of pixels like the number of baselines, N^2 . The detector noise therefore becomes ever more important. However, in the case of a system without background and detector noise ($\sigma_{\text{sky}} = 0$), the ultimate sensitivity of the fringe tracker can be established at 1 photon per coherence time and per telescope, whatever the number of telescopes. For the VLTI, assuming 8-meter telescopes, a coherence time of

10 ms, a throughput of 1 %, and using the full K-band, the ultimate sensitivity is $K_{\text{mag}} = 17.5$. Even assuming the need for an SNR of 1.5 per baseline and per coherence time, we should be able to reach a K_{mag} of 16 (Fig. 11).

So what can be done? To reach this magnitude, there are several paths forward. The first one is to decrease the background and detector noise. The sky brightness in the K-band at Paranal is around 12.8 mag/square arcsec³. Therefore, the fraction of sky background light entering the 60 mas single-mode fiber is almost negligible ($K_{\text{mag,sky}} \leq 19$). A more important light emitter is the VLTI thermal background due to the $\approx 75\%$ absorption of the optical surfaces. All of these surfaces are typically around $T = 283$ K to 288 K, and will contribute to the majority of the background light. Regarding the detector noise, even if the SAPHIRA detector has a readout noise below $1 e^-$, the number of pixels used by the fringe tracker per telescope is 36 (72 in split polarizations). For faint objects, this noise can therefore dominate. Solutions to use less pixels have been proposed (Petrov et al. 2014, 2016) and could lead to a better sensitivity. The development of infrared detectors could also be a promising path forward.

The second path is to increase the coherent throughput. On average, only 1% of the total flux reach the fringe tracker detector. The 20 mirrors between M1 and the GRAVITY cryostat absorb up to 75% of the light. Also, 50% of the light is scattered inside the IO beam combiner, 50% is lost by using the beam-splitter on the on-axis mode, and 50% because of the amplification of the detector (the so-called multiplicative noise). The last part ($\approx 60\%$ of the remaining flux) is lost when injecting the light into the single mode fiber. Throughput improvements could therefore come from using less optical elements and possibly switching more of the mirrors involved from aluminium to gold coatings. Focus can also be put into a more efficient light coupling into the single mode fiber. It would mean a better AO system for a better Strehl. The advantages of a good Strehl are manifold. It increases the mean throughput. It also maximizes the fringe contrast by giving a better instantaneous flux equilibrium. Last, it avoids flux drop-out which are detrimental for good fringe tracking and model prediction.

Third, but not least, a special care shall be taken on the monitoring and removal of the vibrations. The vibrations cause two main sources of problems. Because they are usually at high frequency, they are difficult to predict and affect the fringe tracking performance (by opposition of the atmospheric perturbations which are easier to correct because at lower frequency). But the main problem is they are limiting how slow the fringe tracker can run because the decrease of fringe contrast hurts more than the additional integration time.

8.2. Have we reached the ultimate accuracy?

A false assumption is also that sensitivity can be gained by trading accuracy for sensitivity. The conceptual idea behind that is the former idea that the group delay is sensitive but not accurate, while the phase delay is accurate but not sensitive. However, by simultaneously using the group delay and the phase delay, it is possible to have the best of both. In the dual controller used by GRAVITY, group delay takes care of the coherencing, and phase delay does the phasing.

With GRAVITY, despite the high sensitivity, we are routinely tracking high SNR fringes within 100 nm residual rms. However, when the coherence time is short ($\tau_0 < 3$ ms at 500 nm), the

³ Table 6 in https://www.eso.org/observing/etc/doc/skycalc/The_Cerro_Paranal_Advanced_Sky_Model.pdf

fringe tracker performance degrades (Fig. 12). This is caused by the open loop latency of the fringe tracker (of the order of 4 ms). Observing during these conditions could clearly benefit from a faster fringe tracker. But during good atmospheric conditions, could we still improve the control loop?

Yes. It lies in the proper management of the Kalman filter. For convenience, we used an asymptotic estimation of the Kalman gain from the Riccati equation. A better Kalman filter would propagate errors as well as the states by applying the equation of state also on the covariance matrix:

$$\hat{\Sigma}_{x,n|n-1} = A_V \cdot \hat{\Sigma}_{x,n-1} \cdot A_V^T \quad (77)$$

and derive the optimum gain each DIT. This could be done with addition computing power.

An additional amelioration could come from modal control. It was proposed in Menu et al. (2012) and could theoretically be implemented. However, as of now, we did not find any practical implementation that would make it robust for a realistic environment.

Acknowledgements. SL would like to thank C.Kulcsár, H.-F. Raynaud, J.-M. Conan and L. Mugnier for their insight and remarkable discussions. We acknowledge K. Tristram for his role in operating the instrument and acquiring the data on TYC 5058-927-1 and TYC 7504-160-1. A special thank goes to the pioneering work made by M. Colavita. Part of this work was supported by the European Union under ERC grant 639248 LITHIUM.

References

- Abuter, R., Dembet, R., Lacour, S., et al. 2016, in Proc. SPIE, Vol. 9907, Optical and Infrared Interferometry and Imaging V, 990721
- Berger, D. H., Monnier, J. D., Millan-Gabet, R., et al. 2006, in Proc. SPIE, Vol. 6268, Society of Photo-Optical Instrumentation Engineers (SPIE) Conference Series, 62683K
- Choquet, É., Menu, J., Perrin, G., et al. 2014, A&A, 569, A2
- Colavita, M. M., Booth, A. J., Garcia-Gathright, J. I., et al. 2010, PASP, 122, 795
- Colavita, M. M., Wallace, J. K., Hines, B. E., et al. 1999, ApJ, 510, 505
- Colavita, M. M., Wizinowich, P. L., Akeson, R. L., et al. 2013, PASP, 125, 1226
- Correia, C., Raynaud, H.-F., Kulcsár, C., & Conan, J.-M. 2008, in Proc. SPIE, Vol. 7015, Adaptive Optics Systems, 70151F
- Delplancke, F., Derie, F., Lévêque, S., et al. 2006, in Proc. SPIE, Vol. 6268, Society of Photo-Optical Instrumentation Engineers (SPIE) Conference Series, 62680U
- Finger, G., Baker, I., Alvarez, D., et al. 2016, in Proc. SPIE, Vol. 9909, Adaptive Optics Systems V, 990912
- Genzel, R., Eisenhauer, F., & Gillessen, S. 2010, Reviews of Modern Physics, 82, 3121
- Gravity Collaboration, Abuter, R., Accardo, M., et al. 2017, A&A, 602, A94
- Gravity Collaboration, Abuter, R., Amorim, A., et al. 2018a, A&A, 615, L15
- Gravity Collaboration, Abuter, R., Amorim, A., et al. 2018b, A&A, 618, L10
- Gravity Collaboration, Sturm, E., Dexter, J., et al. 2018c, arXiv e-prints [arXiv:1811.11195]
- Jocou, L., Perraut, K., Nolot, A., et al. 2010, in Proc. SPIE, Vol. 7734, Optical and Infrared Interferometry II, 773430
- Jones, R. H. 1980, Technometrics, 22, 389
- Kiekebusch, M. J., Chiozzi, G., Knudstrup, J., Popovic, D., & Zins, G. 2010, in Proc. SPIE, Vol. 7740, Software and Cyberinfrastructure for Astronomy, 77400T
- Kulcsár, C., Massioni, P., Sivo, G., & Raynaud, H.-F. G. 2012, in Proc. SPIE, Vol. 8447, Adaptive Optics Systems III, 84470Z
- Labeyrie, A. 1970, A&A, 6, 85
- Lacour, S., Dembet, R., Abuter, R., et al. 2018, in Society of Photo-Optical Instrumentation Engineers (SPIE) Conference Series, Vol. 10701, Optical and Infrared Interferometry and Imaging VI, 1070107
- Lacour, S., Eisenhauer, F., Gillessen, S., et al. 2014a, A&A, 567, A75
- Lacour, S., Jocou, L., Moulin, T., et al. 2008, in Proc. SPIE, Vol. 7013, Optical and Infrared Interferometry, 701316
- Lacour, S., Tuthill, P., Monnier, J. D., et al. 2014b, MNRAS, 439, 4018
- Le Bouquin, J.-B., Bauvir, B., Haguenaer, P., et al. 2008, A&A, 481, 553
- Malbet, F., Kern, P., Schanen-Duport, I., et al. 1999, A&AS, 138, 135
- Menu, J., Perrin, G., Choquet, E., & Lacour, S. 2012, A&A, 541, A81
- Perraut, K., Jocou, L., Berger, J. P., et al. 2018, A&A, 614, A70
- Petit, C., Conan, J.-M., Kulcsár, C., Raynaud, H.-F., & Fusco, T. 2008, Optics Express, 16, 87
- Petrov, R. G., Boskri, A., Bresson, Y., et al. 2016, in Proc. SPIE, Vol. 9907, Optical and Infrared Interferometry and Imaging V, 99071F
- Petrov, R. G., Elhalkouj, T., Boskri, A., et al. 2014, in Proc. SPIE, Vol. 9146, Optical and Infrared Interferometry IV, 91462P
- Petrov, R. G., Malbet, F., Weigelt, G., et al. 2007, A&A, 464, 1
- Pfuhl, O., Eisenhauer, F., Haug, M., et al. 2010, in Proc. SPIE, Vol. 7734, Optical and Infrared Interferometry II, 77342A
- Pfuhl, O., Haug, M., Eisenhauer, F., et al. 2014, in Proc. SPIE, Vol. 9146, Optical and Infrared Interferometry IV, 914623
- Pfuhl, O., Haug, M., Eisenhauer, F., et al. 2012, in Proc. SPIE, Vol. 8445, Optical and Infrared Interferometry III, 84451U
- Poyneer, L. A. & Véran, J.-P. 2010, Journal of the Optical Society of America A, 27, A223
- Shao, M. & Colavita, M. M. 1992, A&A, 262, 353
- Tatulli, E., Millour, F., Chelli, A., et al. 2007, A&A, 464, 29
- Weigelt, G. 1977, OptCommun, 21, 55
- Woillez, J., Akeson, R., Colavita, M., et al. 2012, PASP, 124, 51